Correspondence to:
T. M. Powell,
tylerpowell@ucla.edu

High-Resolution Nighttime Temperature and Rock Abundance Mapping of the Moon Using the Diviner Lunar Radiometer Experiment With a Model for Topographic Removal

T. M. Powell[1] , **T. Horvath[1]** , **V. Lopez Robles[1]**, **J.-P. Williams[1]** , **P. O. Hayne[2]** , **C. L. Gallinger[3]** , **B. T. Greenhagen[4]** , **D. S. McDougall[5]**, and **D. A. Paige[1]**

[1]Department of Earth, Planetary, and Space Sciences, University of California, Los Angeles, Los Angeles, CA, USA, [2]Department of Astrophysical and Planetary Sciences, University of Colorado Boulder, Boulder, CO, USA, [3]Department of Earth Sciences, University of Western Ontario, London, ON, Canada, [4]Johns Hopkins University Applied Physics Laboratory, Laurel, MD, USA, [5]Department of Geological Sciences, Brigham Young University, Provo, UT, USA

Abstract The Diviner Lunar Radiometer Experiment on the Lunar Reconnaissance Orbiter (LRO) has been mapping the surface temperatures of the Moon since 5 July 2009. Diviner has since collected over 500 billion radiometric measurements with excellent spatial and local time coverage. However, the most recently published high-resolution Diviner global maps only use data collected from 2009 to 2016. In this work, we compile ~13 years of Diviner data to produce improved global maps of nighttime brightness temperature, bolometric temperature, regolith temperature, and rock abundance (RA). Errors in Diviner's pointing have been corrected and past effective field of view modeling has been optimized to improve data georeferencing without spatial interpolation. We estimate an effective resolution of ~330 m longitudinally and ~700 m latitudinally at the equator, which corresponds to an improvement of ~3.5× longitudinally and ~1.3× latitudinally. In addition, we develop a thermal model that accounts for indirect scattering and emission from surrounding topography. The resulting temperature anomaly maps better highlight variations in temperature caused by thermophysical properties by removing most topographic effects. These improvements allow for the identification of smaller and fainter thermal features than was previously possible. The improved effective resolution of Diviner maps allows for excellent spatial correlation with other high-resolution data sets. To demonstrate this, we compare Diviner RA to a manual survey of boulders in the Apollo 17 landing site region. We show that Diviner RA correlates well with the areal fraction of rocks larger than ~1–2 m in diameter visible in LRO Camera imagery.

Plain Language Summary The Diviner Lunar Radiometer Experiment on board the Lunar Reconnaissance Orbiter has been mapping the temperature of the lunar surface since 5 July 2009. Past Diviner data has been used to produce global maps of nighttime temperature and to determine the thermal properties of the surface. However, the most recently published global maps only used data collected from 2009 to 2016. We recreate these global maps using all data available through July 2022: over 5 years of additional data. We implement several improvements, including a correction for errors in instrument pointing, which result in an increase in effective resolution of ~3.5× and ~1.3× in the longitudinal and latitudinal directions, respectively. This allows lateral brightness temperature variations to be resolved at a finer scale than was previously possible. In addition, we develop a model that mostly removes the effect of topography on nighttime temperatures. The resulting maps better highlight differences in temperature that are caused by variations in the thermal properties of the surface.

1. Introduction

The Diviner Lunar Radiometer Experiment on the Lunar Reconnaissance Orbiter (LRO) has been mapping the reflected solar and emitted infrared radiation of the Moon since 5 July 2009 (Paige, Foote, et al., 2010). Since that time, Diviner has collected over 500 billion radiometric measurements. The Diviner data set has been used to create global and regional maps of surface temperature, derived thermophysical properties, and composition (Bandfield et al., 2011; Greenhagen et al., 2010; Hayne et al., 2017; Lucey et al., 2021; Paige, Siegler, et al., 2010; Williams et al., 2017, 2019, 2022). However, the most recently published 128 pixel-per-degree (ppd) global maps (Bandfield et al., 2017; Greenhagen et al., 2011; Hayne et al., 2017) do not use data collected more recently than 2016.

In this work, we compile ∼13 years of Diviner data to produce updated nighttime brightness temperature, bolometric temperature, regolith temperature, and rock abundance (RA) maps of the Moon, which extend to ±70° latitude. The greater data volume results in substantially increased spatial and local time coverage. In addition, we implement several improvements which result in noticeably sharper maps with fewer data artifacts: (a) Errors in instrument pointing have been corrected, resulting in better georeferencing of Diviner measurements; (b) past effective field of view (EFOV) modeling (Williams et al., 2016) used to determine the center of each Diviner observation accounting for topography and spacecraft motion has been optimized to produce sharper maps; and (c) curve fitting of nighttime temperatures is used to calculate temperatures at a uniform local time. These updates allow for the exploration of the lunar thermal environment at a much finer scale than was previously possible.

Nighttime surface temperatures are strongly influenced by thermophysical properties, often characterized by thermal inertia, which describes a material's resistance to changing temperature. High thermal inertia materials (e.g., rock) remain warmer throughout the night than lower thermal inertia materials (e.g., regolith). However, topography also affects surface temperatures. Local slopes influence the amount of direct solar illumination received by a particular surface, and the surrounding topography can scatter and emit radiation onto a surface, which results in additional indirect heating (Aharonson & Schorghofer, 2006; Paige et al., 1994). It is often desirable to remove the effect of topography on nighttime temperature to better highlight variations in temperature that are caused by thermophysical properties. In this work, we present a model for topographic removal that accounts for scattered and emitted radiation from surrounding surfaces.

## 2. Data and Methods

2.1. Diviner Data Set

Diviner is an infrared radiometer with nine spectral channels covering a wavelength range of 0.3–400 μm (Paige, Foote, et al., 2010). Channels 1 and 2 (0.3–3.0 μm) measure solar reflectance, channels 3–5 (7.80 ± 0.25, 8.20 ± 0.25, and 8.60 ± 0.20 μm) measure the peak of the Christiansen thermal emission feature (Conel, 1969), which is indicative of silicate mineralogy (Greenhagen et al., 2010), and channels 6–9 (13–23, 25–41, 50–100, and 100–400 μm) measure thermal emission over the wide range of lunar surface temperatures. Each channel consists of a 21-element thermopile detector array. Diviner normally operates as a nadir-pointing pushbroom mapper, though it can point off-nadir for targeted observations.

We collected Diviner Reduced Data Records (RDRs) for channel 6–9 from the start of the mission (July 2009) through July 2022. Data were restricted to emission angles less than 15° to avoid phase-angle dependent thermal emission behavior (Bandfield et al., 2015; Warren et al., 2019). We also employ several constraints on data quality described in the Diviner RDR's documentation (Sullivan et al., 2013): quality flag for calibration—0, quality flag for miscellaneous—0, noise quality flag—0–1.5, and activity flag—110–192. Diviner radiance measurements were binned at 128 pixels-per-degree, which corresponds to ∼237 m at the equator, and in 0.25 lunar hour time steps. Binned radiance values were then converted to brightness temperatures.

2.2. Correction of Angular Pointing Offsets

In 2019, it was found that the Diviner instrument had been experiencing a systematic cross-track pointing offset since the start of the mission. This was discovered when analyzing features that were smaller than the effective field-of-view (EFOV) of a Diviner observation, such as lunar collapse pits (Horvath et al., 2019, 2022) and small rocky craters. These small, sub-resolution features should contribute to the temperature of only one spatial bin when gridded at 128 ppd; however, such features were observed to be several spatial bins wide in nighttime temperature maps derived from binning data throughout the night. Further investigation revealed that the apparent location of these features varied slightly in longitude for different orbits due to an unknown angular pointing error in Diviner's elevation actuator in the cross-track direction.

To characterize the angular pointing offset, we tracked the apparent location of several candidate targets throughout the duration of the mission. Suitable targets were selected based on the following criterion: (a) about the size of or smaller than the EFOV of a single Diviner observation and (b) thermally pronounced from their surroundings throughout the night. We selected 13 targets consisting of lunar collapse pits and small rocky craters ranging in size from 100 to 300 m. We retrieved all channel 6–7 Diviner data with <10° emission angles and manually measured the offset between their apparent location and the true target location in LRO Camera (LROC) Narrow Angle Camera (NAC) imagery. This was converted to an angular offset by accounting for spacecraft altitude and
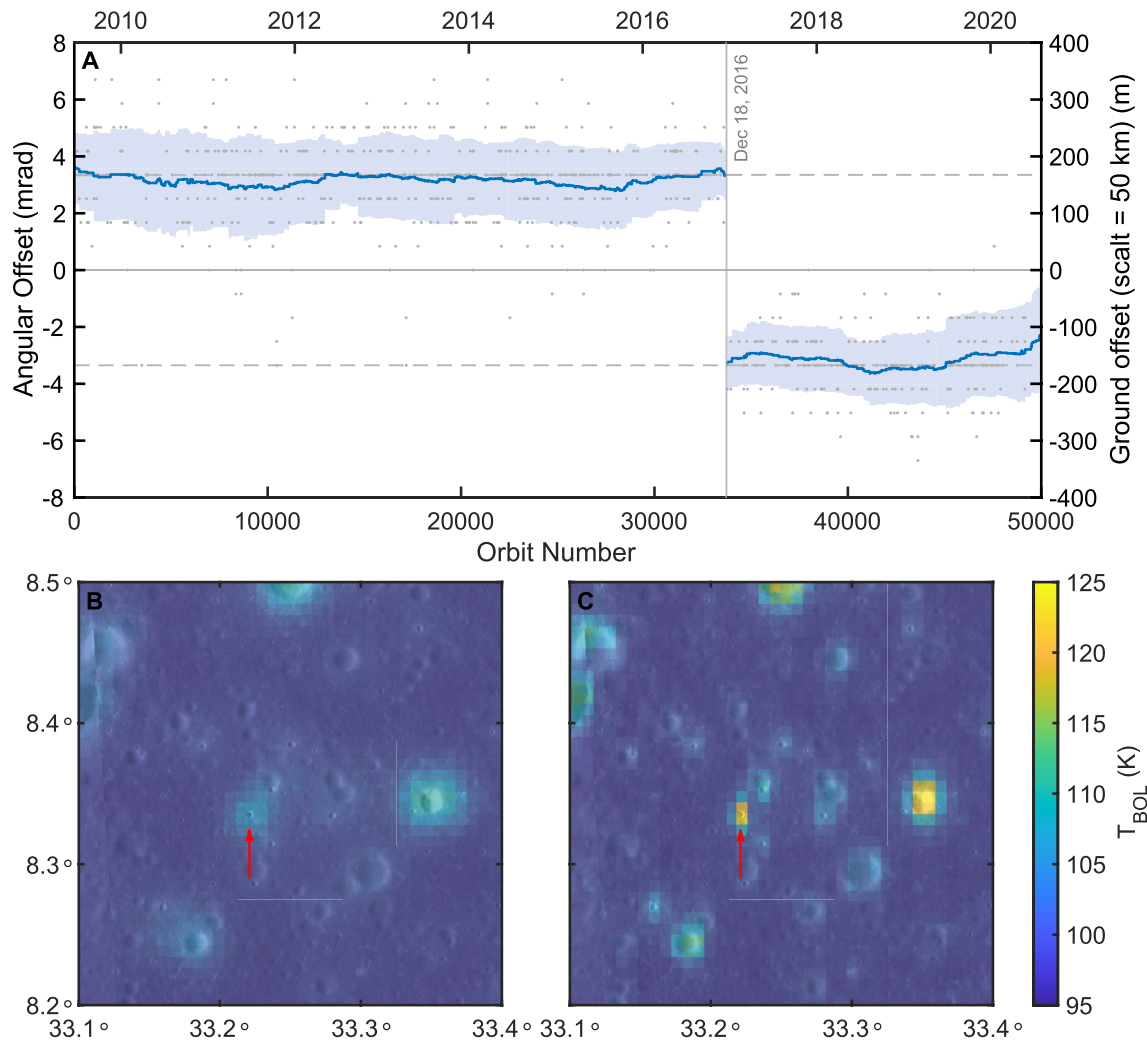
Figure 1. (a) Cross-track angular offset versus time for Diviner where the positive and negative cross track direction is defined relative to the Diviner detector array. From the start of the mission until December 2016, Diviner observations were offset by ~3.4 mrad. After December 2016 the detector offset was also ~3.4 mrad, but in the opposite cross-track direction. The blue line was constructed using a rolling average with a window of 5,000 orbits. (b, c) Example of midnight bolometric temperatures for a region (b) before and (c) after the angular offset correction in panel (a) and the updated effective field-of-view modeling approach (Section 2.3) are applied. After correction, warm spatial bins correspond more accurately to geologic features like rocky impact craters, and the temperature magnitude is more pronounced. The warm feature at 8.33°N and 33.22°E (red arrow) is a lunar collapse pit.

orientation. On average, there were ~25 observations per target per channel. Figure 1a shows the trend of the angular offset magnitude and direction throughout the mission duration. The offset was approximately constant at ~3.4 mrad in the positive cross-track direction (defined relative to the Diviner detector array) from the start of the mission until December 2016. This is equivalent to a ground-projected offset of ~170 m at a spacecraft altitude of 50 km, or ~70% of an equatorial 128 ppd spatial bin. Although the offset was roughly constant during this period, this does not mean that targets were simply shifted in early Diviner maps. LRO occasionally performs 180° yaw flips to maintain the Sun on the solar array side of the spacecraft, resulting in the detector arrays reversing direction relative to the spacecraft in-track direction (Tooley et al., 2010). Therefore, a target's apparent location can vary by ~3.4 mrad from its true location in either longitudinal direction when binned spatially, depending on the orientation of the spacecraft. In December 2016, the angular pointing offset abruptly shifted to ~3.4 mrad in the negative cross-track direction. This was found to correspond with the Diviner instrument temporarily entering safe mode from 15 to 18 December 2016 after registering multiple actuator position errors.

Offsets in the georeferencing of Diviner observations leads to blurring of features, hence decreasing the effective resolution of the measurements when creating binned maps. This is especially apparent for small features and sharp thermal contrasts. Data from a particular point on the surface will pollute adjacent bins, suppressing

unique thermal signals, and causing sharp thermal boundaries to become blurred. Luckily, because the angular pointing error has been fairly predictable with time, we can use the results of Figure 1a as a calibration to properly georeference Diviner data. The result of this correction applied to Diviner bolometric temperature is shown in Figures 1b and 1c. This lunar mare example region contains several rocky craters and a lunar collapse pit (8.33°N, 33.22°E) which have elevated nighttime temperatures. Figure 1b shows the bolometric temperature at midnight without correcting for the Diviner pointing offsets or using the updated approach to EFOV modeling, which we discuss in Section 2.3. In this map, thermal features are smeared in the longitudinal direction and temperatures are muted because of incorrectly georeferenced observations originating from neighboring spatial bins. Figure 1c shows the same region but applies the pointing correction and the updated EFOV modeling approach (Section 2.3). With these improvements applied, thermal features are properly localized to their corresponding geologic features. While both maps are binned at 128 ppd, the ability to resolve smaller features in the new maps demonstrates an increase in effective resolution. For example, the apparent size of the temperature feature associated with the lunar collapse pit is ∼3–4 pixels wide before the corrections are applied and ∼1–2 pixels wide afterward. Additionally, the thermal contrast between warm and cool regions is substantially improved, allowing fainter thermal features to be identified than was previously possible.

2.3. Effective Field-Of-View Modeling

Diviner data is typically stored as a point-based data set with measurements centered at the temporal midpoint of the observation. This sometimes results in gaps in data when spatially binning, especially when the LRO spacecraft is at a greater altitude. Williams et al. (2016) presents a method for determining the ground-projected EFOV of a Diviner measurement accounting for spacecraft viewing geometry and motion, surface topography, and the thermal response time of each detector. Figures 2a–2c shows the ground projected footprint of a single Diviner channel 7 detector measurement at several spacecraft altitudes. In past maps, spatial bins which were within the EFOV of a measurement but did not contain the center-point of the measurement were populated with data. This allowed all bins within the ground track observed by Diviner to be filled in, which was necessary for previous Diviner products to achieve sufficient spatial coverage. However, this can result in some blurring due to averaging of radiances from adjacent overlapping EFOVs, particularly at sharp boundaries in temperature. In this work, we use the Williams et al. (2016) method to find the center-point of each Diviner observation's EFOV, but we do not populate neighboring bins. This is now possible because of the greater data volume from ∼13 years of Diviner observation. The resulting maps benefit from a reduction in averaging between overlapping observations that better isolates the individual brightness temperature measurements while the higher density of the current data provides adequate spatial coverage to eliminate gaps in binned data at this resolution. This approach, along with the correction to the Diviner pointing errors, results in noticeably sharper temperature maps.

To demonstrate the improvement in map sharpness, we model the "spatial response function" (SRF) for a 128 ppd spatial bin considering that the value of a particular spatial bin is constructed by averaging several Diviner observations which have their own unique EFOV. For eight equatorial locations, we collect all Diviner data recorded throughout the duration of the mission and simulate the EFOV of each individual detector measurement accounting for the location of the observation, spacecraft and detector array orientation (traveling either north-south or south-north), spacecraft velocity, and spacecraft altitude (Williams et al., 2016). To produce the SRF, the EFOV of all measurements are weighted by the proportion that they contribute to the target pixel and are summed. Figure 2d simulates the SRF of the previously published Diviner maps, where pointing offsets are not corrected for and Diviner measurements centered outside of the target spatial bin contribute to the value of the bin. The black contour outlines the region that contributes to 50% of the total response. We define the extent of this region as the effective resolution. This shows that the equatorial effective resolution of the previously published Diviner maps is ∼1.15 km by ∼920 m in the longitudinal and latitudinal directions, respectively. For reference, the nominal size of a 128 ppd spatial bin at the equator is ∼237 m in both directions. Figure 2e uses the same EFOV modeling approach as Figure 2d but includes a correction for pointing offsets. Figure 2f both corrects for pointing offsets and uses the updated EFOV modeling approach, where only observations whose centers fall within the target spatial bin are considered. The effective resolution of a spatial bin at the equator following this method is ∼330 by ∼700 m in the longitudinal and latitudinal directions, respectively. This constitutes an improvement of ∼3.5× longitudinally and ∼1.3× latitudinally.

The effective resolution of a spatial bin is also expected to vary in size with latitude due to differences in spacecraft altitude. During the first ∼2 years of operation, LRO was in a near-circular polar orbit with an average
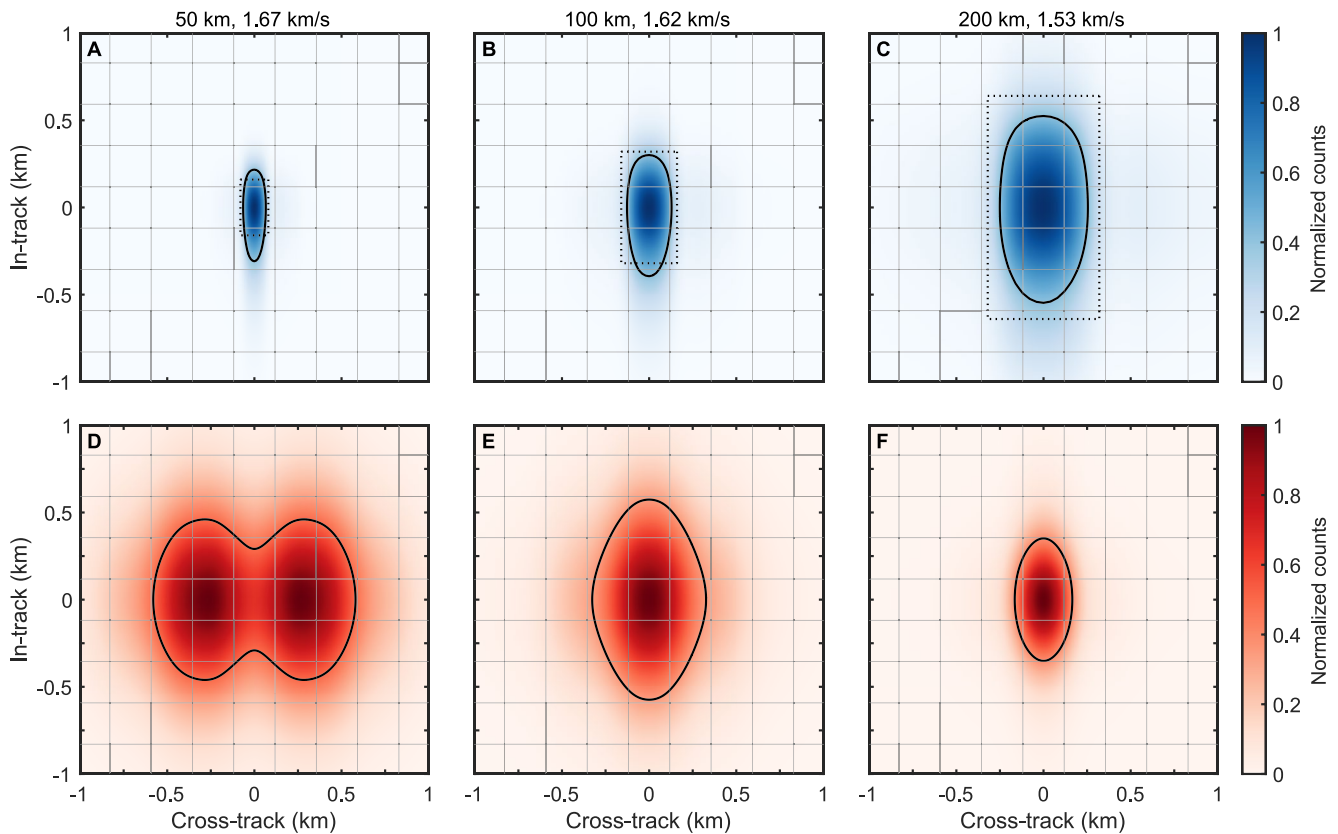
Figure 2. (a–c) The effective field-of-view of a Diviner detector observation at several spacecraft altitudes. The black contours outline the region within which 50% of the observation response originates. The gray lines represent a 128 pixel-per-degree (ppd) grid at the equator, and the dotted rectangle shows the nominal instantaneous field of view of a Diviner detector (Paige, Foote, et al., 2010; Williams et al., 2016). (d–f) The modeled spatial response function for an equatorial 128 ppd spatial bin, constructed for the following approaches: (d) no correction for detector offsets and neighboring observations contribute to the target spatial bin's response; (e) offsets are corrected and neighboring observations contribute to the target spatial bin's response; and (f) offsets are corrected and only observations centered within the target spatial bin contribute to the bin's response.

altitude of ~50 km (Mazarico et al., 2012, 2018). LRO then transitioned to a quasi-frozen elliptical orbit with periapsis near the South Pole and spacecraft altitude varying between ~30 and ~180 km, and the orbit has continued to evolve throughout the duration of the mission (Mazarico et al., 2018). In general, this results in higher effective resolution in the southern hemisphere and lower effective resolution in the northern hemisphere. This is demonstrated in Figure 3, which shows the simulated effective resolution in the longitudinal and latitudinal directions as a function of latitude.

2.4. Slope-Adjusted Midnight Brightness Temperature

We create brightness temperature maps for channels 6–9 by calculating the temperature at a particular local time from the nighttime data using non-linear curve fitting. For each channel and 128 ppd spatial bin, we fit the nighttime cooling curve with an exponential function of the form: $T_B = Ae^{B/t} + C$ where T_B is brightness temperature, t is local time, and A, B, and C are constants (Figure 4). This form was chosen empirically, as it reproduces the cooling curves on the Moon better than other simple mathematical forms (e.g., linear or polynomial). Data within half an hour of sunrise and sunset are excluded to avoid the complex illumination conditions that can occur near the terminator because of topography. We require that the spatial bins have at least three nighttime observations, with at least one observation occurring both before and after midnight. Spatial bins that do not meet these criteria are assigned as null values. A typical 128 ppd spatial bin has ~14 nighttime observations per channel which are used for fitting (Figure 4), and only ~0.003% of spatial bins do not meet the fitting criteria. The median fit standard error for each channel is 2.24 K, 0.74 K, 1.13 K, and 2.46 K for channels 6, 7, 8, and 9, respectively. The best-fit cooling curve is then used to calculate the brightness temperature at a particular local time. We
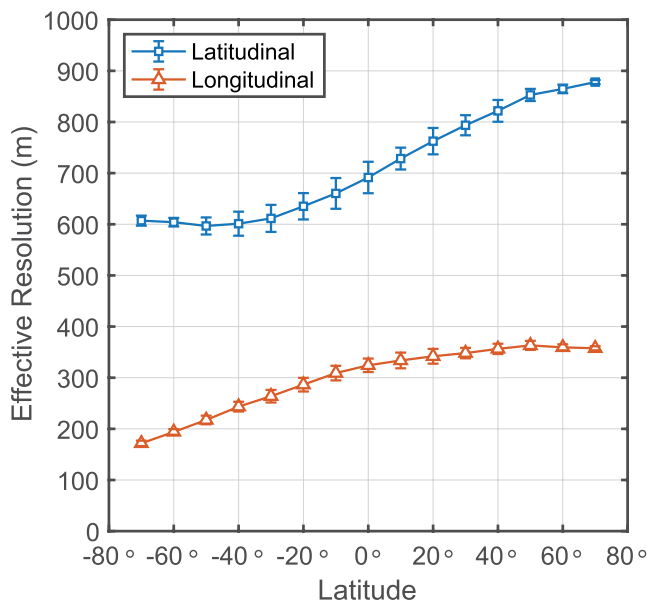
Figure 3. The effective resolution of a 128 pixel-per-degree spatial bin in the longitudinal and latitudinal direction as a function of latitude. The marker at each latitude shows the average and standard deviation of the effective resolution determined for eight locations with varying longitude at that latitude.

produce brightness temperature maps for channels 6–9 at two local times: local midnight and "slope-adjusted midnight."

For flat surfaces, slope-adjusted midnight is equivalent to local midnight. However, for surfaces sloped in the east-west direction, the time of peak solar illumination is shifted in local time. To first order, the resulting diurnal temperature curve can be approximated by shifting the timing of the diurnal temperature curve of a flat surface by the local east-west slope angle (Hayne et al., 2017). The local slope angle is determined using the 128 ppd SLDEM 2015 topographic map, which merges SELENE Kaguya TC and LRO Lunar Orbiter Laser Altimeter elevation data (Barker et al., 2016). This correction removes some of the effects of topography on midnight temperatures. Further topographic corrections are discussed in Section 3.

2.5. Bolometric Temperature, Regolith Temperature, and Rock Abundance

A single Diviner observation may contain a distribution of temperatures due to the presence of spatially unresolved rocks and small-scale slopes within the detector FOV. This results in differences in the brightness temperatures recorded by each of the Diviner channels. Regions with a mixture of temperatures have greater brightness temperatures in the shorter wavelength channels. The bolometric temperature (T_{BOL}) approximates the wavelength-integrated flux from all Diviner channels as an equivalent blackbody temperature. This quantity is useful because it represents the total radiative heat flux leaving the surface expressed as an effective temperature. This makes bolometric temperature a good metric for comparison to thermal models, which generally represent the total heat balance of the surface. We use channels 6, 7, 8, and 9 to produce maps of midnight and slope-adjusted midnight bolometric temperature using the method described in Paige, Siegler, et al. (2010).
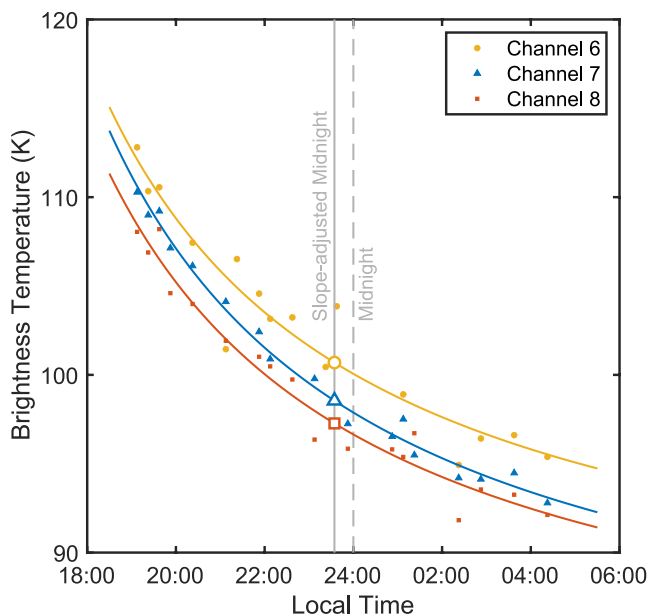
Figure 4. Channels 6–8 nighttime brightness temperature curves at an example location (−176.6523°E, −16.4492°N). Each nighttime curve is fit to an exponential function, which is used to calculate the temperature at midnight and slope-adjusted midnight. The surface has an east-west slope of ~5.3°, so slope-adjusted midnight occurs ~0.35 lunar hours earlier in the night.

The differences in brightness temperature measured by each channel can also be leveraged to probe the sub-resolution mixture of temperatures for aniso-thermal surfaces. Most nighttime anisothermality on the Moon is caused by rocks, which have higher thermal inertia than regolith and remain warmer throughout the night. Unequal heating of small-scale slopes also contributes to anisothermality, but at night, this generally has a smaller effect than the presence of high thermal inertia materials (Bandfield et al., 2015). Bandfield et al. (2011) presents a method for estimating the fraction of rocks larger than ~1 m contained within a Diviner spatial bin. This process was used to produce the previous generation of RA and regolith temperature maps, which we briefly summarize here.

Bandfield et al. (2011) assumes that the surface is made of just two materials: rock and regolith. Rock temperatures are determined using a one-dimensional thermal model assuming the thermophysical properties of vesicular basalt as described by Horai and Simmons (1972), an albedo of 0.15, and a hemispherical emissivity of 0.95 (Bandfield et al., 2011). We construct a lookup table of rock temperatures at midnight and slope-adjusted midnight accounting for latitude, local slope geometry, shadowing, and scattered and emitted radiation from surrounding topography as described in Section 3. For each spatial bin, we then find the mixture of rock and regolith temperatures that best fits the radiances observed by Diviner channels 6–8. This is done by simulating Diviner's spectral response for an imaginary surface with an unknown areal fraction of rock and regolith, where the rock temperature is determined from modeling and the regolith temperature is unknown. The derived RA and regolith temperature (T_{REG}) occur for the combination of these values
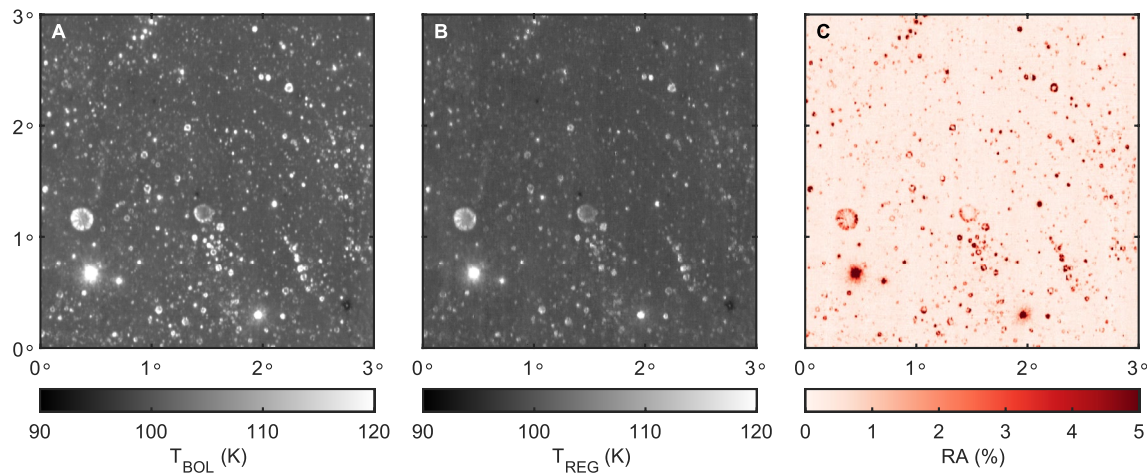
Figure 5. Examples of derived (a) bolometric temperature, (b) regolith temperature, and (c) rock abundance at slope-adjusted midnight.

that best fits the observed channel 6–8 radiance by minimizing RMS differences. We assume a nadir emissivity of unity for both rocks and regolith. Figure 5 shows derived bolometric temperature, regolith temperature, and RA for an example region.

Modeled rock temperatures assume an infinitely thick and laterally continuous layer of rock. This is an appropriate assumption for rocks that are sufficiently larger than the thermal skin depth (~1 m for rock), so the resulting RA should be interpreted as the fraction of the surface covered with rocks larger than ~1 m in diameter. However, it is important to note that this 2-component model is a simplification. In practice, the Diviner FOV may contain several different materials. Small rocks will have a different cooling behavior than large rocks, as they will eventually be cooled laterally by the surrounding regolith. Additionally, if rocks on the Moon have been heavily fractured or are covered by a thin layer of regolith, they may be cooler than a large, coherent rock due to differences in their thermophysical properties. For example, a 10% value in the derived RA map may correspond to a greater areal fraction of regolith covered rocks or small rocks. Additionally, derived regolith temperatures likely include some contribution from small rocks or regolith covered rocks, whose nighttime temperatures may be intermediate between typical regolith and coherent rock (Figure 5b). This can be probed with more complicated models that account for more than two temperature components (Elder et al., 2016). However, this RA metric is a valuable way of interpreting the anisothermality observed by Diviner as a geologically relevant quantity and can be used to compare relative differences in RA between regions.

3. Thermal Model for Topography Removal

Nighttime temperature maps are valuable because they are diagnostic of the thermophysical properties of the surface. However, spatial variations in temperature can also be caused by latitude and topography, so it is often desirable to remove these effects. Here we present a model for topographic subtraction, which uses a one-dimensional thermal model that accounts for latitude, slope, shadowing at sunrise and sunset, and scattered and emitted radiation from surrounding surfaces.

3.1. Direct Solar Illumination

Latitude is the dominant first-order effect that influences lunar surface temperatures, as it affects the solar incidence angle and the amount of direct solar illumination received throughout the day. Figure 6 shows the trend in median midnight bolometric temperature and regolith temperature with latitude for typical lunar regolith (excluding spatial bins with slopes >2° and rock abundances >0.5%). Median midnight bolometric temperatures vary from ~101 at the equator to ~83 K at 70° latitude. Median regolith temperatures are slightly cooler than bolometric temperatures. This difference is due to anisothermality, as the contribution from rocks is mostly removed in the calculation of regolith temperature, but is included in the bolometric temperature. Typical regolith has a low-level background RA of ~0.3%.
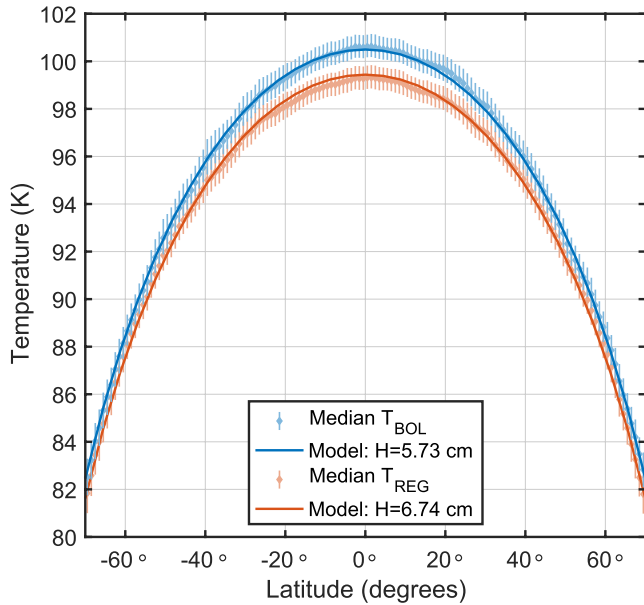
Figure 6. Median T_{BOL} and T_{REG} of flat and non-rocky surfaces (slope < 2° and rock abundance < 0.5%) as a function latitude compared to a one-dimensional thermal model based on Hayne et al. (2017). Error bars represent the interquartile range within each bin.

We fit the trend in midnight temperatures with latitude using a one-dimensional finite volume thermal model based on Hayne et al. (2017). This model describes the vertical density structure of the regolith as an exponential increase in density ρ with depth z (Hayne et al., 2017; Vasavada et al., 2012):

$$\rho(z) = \rho_d - (\rho_d - \rho_s)e^{-z/H} \tag{1}$$

where ρ_s and ρ_d are the densities of the surface and at depth, respectively. The parameter H is an exponential scale height describing the thickness of the loosely packed surface layer. We find that an H of ~6.74 cm best fits the trend of midnight regolith temperature with latitude, which agrees very well with the mean H-parameter calculated by Hayne et al. (2017) of ~6.8 cm using the Bandfield et al. (2017) regolith temperatures. For midnight bolometric temperature, we find an H-parameter of ~5.73 cm.

In addition to latitude, local slope also influences the amount of direct solar illumination received. For example, a 10° pole-facing slope at 20°N latitude will experience the same solar incidence angle at noon as a flat surface located at 30°N latitude. Hayne et al. (2017) implemented a simple correction for slope where the "effective latitude" of a particular spatial bin is shifted from that of a flat surface by the north-south component of the slope. As described in Section 3.1, Hayne et al. (2017) also adjusted the "effective local time" by the east-west component of the slope, which we replicate by calculating the temperature at slope-adjusted midnight.

3.2. Indirect Scattered and Emitted Radiation

Topography can scatter and emit radiation onto surrounding surfaces. This indirect illumination results in additional heating. The radiative balance for a patch of ground that receives scattering and emission from surrounding topography is:

$$Q = Q_{solar} + Q_{emis} + Q_{scat} \tag{2}$$

where the total incoming radiation Q is the sum of direct solar illumination Q_{solar} and indirect illumination from the land in the form of scattered visible Q_{scat} and emitted infrared Q_{emis} radiation. The total amount of thermal emission from the surrounding land received at some time is determined by the radiative flux from each spatial bin within the line of sight of the target spatial bin weighted by the cosine of the incidence angle i and integrated over all spherical angles Ω (Aharonson & Schorghofer, 2006; Helbig et al., 2009; Paige et al., 1994):

$$Q_{emis} = \int \epsilon \sigma T^4 \cdot \frac{1}{\pi} \cos i \, d\Omega \tag{3}$$

where ϵ is emissivity, σ is the Stefan-Boltzmann constant, and T is the temperature of each spatial bin. This can be approximated as:

$$Q_{emis} = \epsilon \sigma T_{land}^4 \cdot \frac{1}{\pi} \int \cos i \, d\Omega = \epsilon \sigma T_{land}^4 \cdot f_{land} \tag{4}$$

where the land view factor f_{land} describes the amount of land within the target spatial bin's line of sight (weighted by $\cos i$), and T_{land} is an equivalent scene temperature which produces the same total emission as the entire scene. A similar equation exists for the incoming scattered visible light:

$$Q_{scat} = A Q_{land} \cdot f_{land} \tag{5}$$

where Q_{land} is the average solar flux incident on each spatial bin within the line of sight weighted by $\cos i$, and A is the albedo of the surroundings.
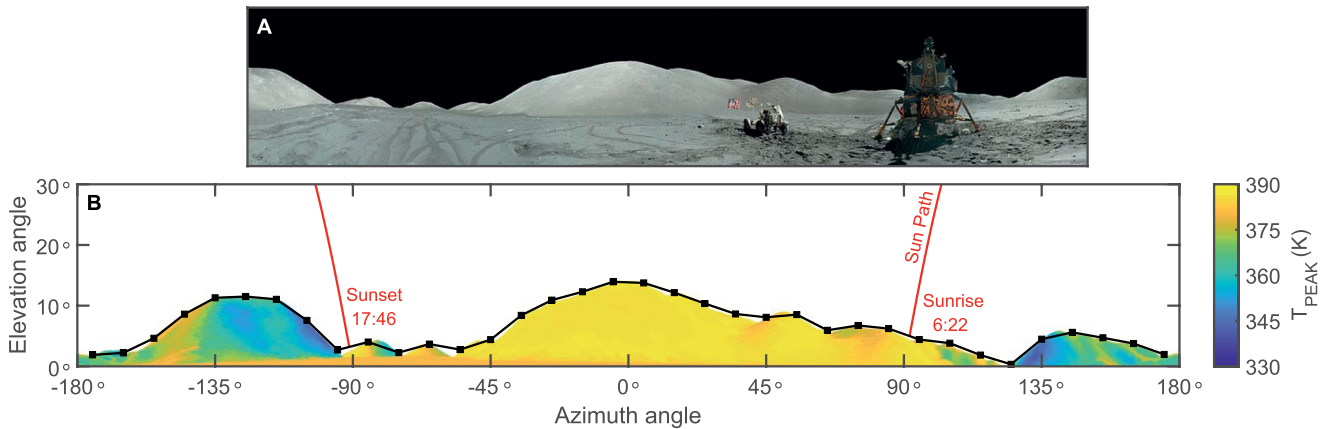
Figure 7. (a) A panorama taken at the Apollo 17 landing site (30.772°E, 20.191°N) and (b) a panorama of the same region constructed using the 128 pixel-per-degree (ppd) SLDEM 2015 topographic map (Barker et al., 2016). Peak temperatures for each 128 ppd spatial bin are calculated assuming radiative equilibrium with solar illumination and the emissivity and albedo values described in Hayne et al. (2017). The horizon profile and peak temperatures are used to calculate f_{land} and T_{land}, which describe the amount of scattered and re-emitted radiation that contribute to the energy balance at the Apollo 17 landing site. While this figure shows all 128 ppd spatial bins within the line of sight, the calculation of f_{land} and T_{land} is approximated by sampling along 10° azimuth angle and 1° elevation angle increments. The horizon profile is also used to calculate the sunrise and sunset times.

First, we use the SLDEM 2015 topographic map (Barker et al., 2016) to calculate f_{land}. The elevation angle α of a distant point above the horizon can be approximated as $\alpha = \arctan\frac{\Delta h}{L} - \frac{\theta}{2}$ where L is the distance to the point and Δh is the difference in elevation. The second term describes the drop-off of the horizon due to the curvature of the Moon, where θ is the central angle subtended by an arc to the distant point which can be calculated using the haversine formula. Figure 7 shows a panorama taken at the Apollo 17 landing site and the same scene constructed using the 128 ppd SLDEM 2015 topographic map. Calculating the elevation angle for every nearby spatial bin as shown in Figure 7 is too computationally expensive to be repeated for every 128 ppd spatial bin on the Moon. Instead, we only calculate elevation angle for spatial bins that lie along rays cast in 10° azimuth angle increments. A horizon profile is constructed by finding the maximum elevation angle along each of these rays (Figure 7), and f_{land} is calculated by numerically integrating the horizon profile weighted by the incidence angle relative to the surface normal (Equation 4).

Next, we calculate the equivalent temperature of the surrounding scene T_{land}. The behavior of the scene temperature throughout the day can be quite complicated, as particular surfaces within the line of sight may experience more solar illumination than others and may become illuminated at different times. Calculating a unique land emission diurnal curve for each spatial bin is computationally expensive and not easily scalable for a global map. However, equivalent scene temperatures throughout the day can be approximated by relating the temperature of the surrounding scene to that of a flat surface at some latitude, which emits a similar total flux.

The peak temperature T_{peak} at slope-adjusted noon for each spatial bin within the line of sight is easily calculable based on their latitude and slope angle (Section 3.1) by assuming radiative equilibrium with solar illumination (Figure 7). We use the nominal emissivity and albedo values described in Hayne et al. (2017) which were found to be appropriate for the Moon on average, though this may introduce uncertainties in the surrounding temperatures due to regional differences in albedo and emissivity. We calculate the equivalent scene temperature T_{land} by sampling T_{peak} along rays cast in 10° azimuth angle increments and 1° elevation angle increments. The total flux from land emission Q_{emis} is calculated by numerically integrating Equation 3. Equation 4 is then solved for T_{land}, which is a single scene temperature that produces the same total radiative flux as the entire scene. This equivalent temperature represents the maximum instantaneous emission received from each spatial bin within the line of sight at slope-adjusted noon. To estimate the emitted flux received at other times of the day, we determine the characteristic latitude ϕ_{land} which has the same maximum temperature. We use a one-dimensional thermal model (Section 3.1) to approximate the diurnal temperature curve throughout the day at this characteristic latitude. This is also used to determine the solar illumination of the scene throughout the day Q_{land}. While this method does not account for differences in the timing of illumination within the line of sight, it does approximate the total flux received from each surrounding spatial bin throughout the day.
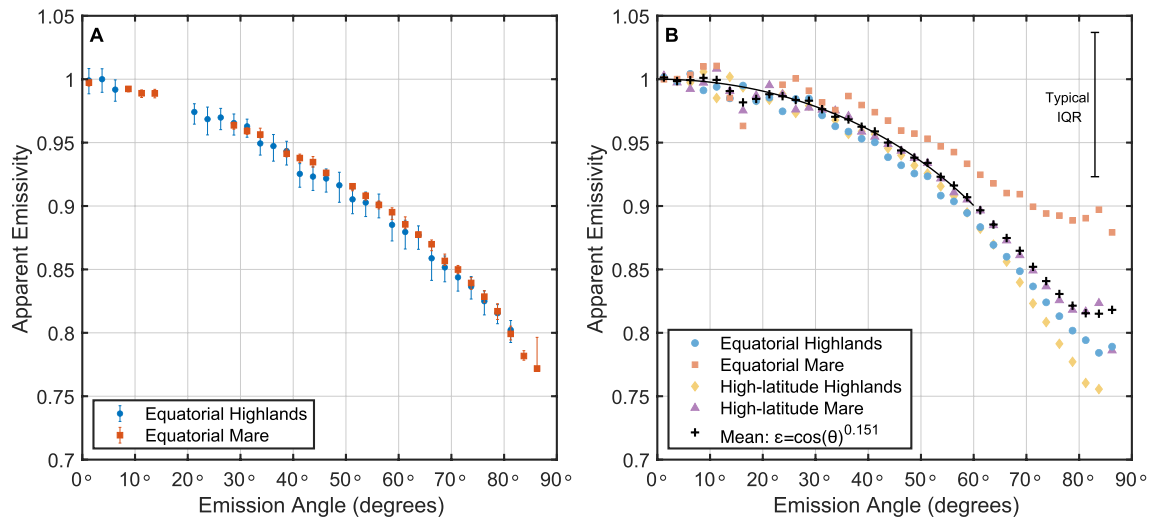
Figure 8. (a) Median Diviner broadband apparent emissivity as a function of emission angle at noon for two equatorial targets. We constrain solar incidence angle to <2°. We assume a nadir emissivity of ∼1 at 0° emission angle. Error bars represent the interquartile range of each bin. (b) Median broadband apparent emissivity around midnight (22:00–02:00 local time) for the same two equatorial targets as well as two targets at ∼50°N latitude. For clarity, the error bar in the upper-right shows the typical interquartile range. The nighttime average apparent emissivity is fit to an empirical function between 0° and 60° emission angle.

Lastly, regions that are at the bottom of steep topography may also experience shadowing at sunrise and sunset, which reduces the total amount of illumination received throughout the day. We calculate the time of sunrise and sunset by finding the intersection of the horizon profile with the path of the sun in the sky (Figure 7).

3.3. Selection of Albedo and Emissivity for Land Scattering and Emission

The amount of emitted and scattered illumination radiated from the surroundings and absorbed by a patch of ground depends on the albedo and emissivity. Diviner results and photometric studies have shown that regolith is not a lambert scatter or emitter; apparent albedo and emissivity vary with the incidence angle of incoming solar illumination, and the azimuth and emission angle of the measurement (Bandfield et al., 2015; Foote et al., 2020; Rubanenko et al., 2020; Warren et al., 2019; Winter & Krupp, 1971). This is often attributed to sub-resolution surface roughness, which causes small-scale variations in illumination and shadowing. Typical slopes in the lunar highlands are <10° with slopes rarely exceeding 30° (Rosenburg et al., 2011), so most land emission and scattering comes from low in the sky. It is therefore necessary to select values of albedo and emissivity that are appropriate for these very high emission angles.

Foote et al. (2020) presents laboratory measurements of the directional albedo of Apollo soils at various incidence angles. We select a value of albedo of 0.15 which corresponds to the apparent albedo of Apollo 16 soil at ∼80° emission angle for a nadir-illuminated target. Diviner has been performing systematic off-nadir observations at several points on the Moon to characterize the emission phase function of the lunar surface (Bandfield et al., 2015; Greenhagen et al., 2017). We look at off-nadir Diviner bolometric temperature measurements for two equatorial sites: highlands (141.39°E, 0.36°N) and mare (−54°E, −0.6°N). The solar incidence angle was constrained to <2°. Figure 8a shows the drop-off in apparent emissivity with emission angle relative to an assumed nadir apparent emissivity of 1. We select an emissivity of 0.8, which corresponds to the apparent emissivity of nadir-illuminated lunar regolith at ∼80° emission angle as measured by Diviner.

The emission and reflectance phase functions of illuminated surfaces also depend on the solar incidence angle, so assuming a constant value of albedo and emissivity is a simplification. At high solar incidence angles, small-scale sun facing slopes will receive more illumination than slopes facing away from the sun. As a result, the apparent emissivity becomes azimuthally anisotropic, with higher and lower apparent emissivity when viewed from the sun and anti-sun directions, respectively. This effect is most important at high-latitudes, where the sun is at high solar incidence angle throughout the day. However, the approximation of a constant emissivity works fairly well for equatorial and mid-latitude locations where noon solar incidence angles are close to 0°. Further study of the emission and reflectance phase function can help to better inform future models.

The emission phase function also influences the radiances measured by Diviner. When Diviner is nadir-pointing, sloped surfaces will be viewed at emission angles equivalent to their local slope angle. Figure 8b shows the nighttime emission phase function (22:00–02:00 local time) for the two equatorial sites as well as a high-latitude mare (−71.52°E, 52.97°N) and a high-latitude highlands (−109.55°E, 49.55°N) location. All locations show a decrease in emissivity with emission angle. Interestingly, the nighttime emission phase function is azimuthally isotropic, indicating that it does not retain significant information about the illumination history of the surface. The equatorial mare location drops off less rapidly with emission angle than the other locations. This may be due to the higher average RA at the location, as rocks remain warmer at night and may influence the temperatures measured by Diviner when viewed off-nadir. However, these regions generally show a similar behavior. We fit the average nighttime emission phase function to an empirical function: $\varepsilon = \cos(\theta)^{0.151}$, where the apparent emissivity drops from 1 at nadir to ∼0.98 at 30° emission angle. While a small effect, this indicates that Diviner should measure slightly reduced brightness temperatures on steeply sloped surfaces. We include this slope-dependent nighttime emissivity in our modeled temperatures to match the brightness temperatures measured by Diviner more accurately.

3.4. Topographic Subtraction

We use a one-dimensional finite volume model to determine the expected nighttime temperature for each point on the Moon. We use the same thermophysical and photometric properties described in Hayne et al. (2017) except for H-parameter, which we set to 5.73 cm for modeling bolometric temperature and 6.74 cm for modeling regolith temperature (Figure 6). We create a lookup table of modeled temperature at slope-adjusted midnight for typical regolith accounting for the following parameters: latitude, slope angle and azimuth, land view factor, effective latitude of the surroundings, and sunrise and sunset times. The expected slope-adjusted midnight temperature, assuming typical regolith properties, is then determined for each spatial bin by querying this lookup table. The difference between the measured Diviner temperature and the modeled temperature is the temperature anomaly ΔT. If topography is properly accounted for, ΔT should show only the effect of thermophysical properties on nighttime temperature.

Figure 9 shows ΔT_{BOL} for a region at equatorial to mid-latitudes (0°–40°N) with progressively increasing levels of topographic removal: (a) latitude correction, (b) simple slope correction, and (c) land scattering and emission correction. Most large-scale topographic features are removed by the simple slope correction, which is equivalent to the slope correction applied in the Hayne et al. (2017) global H-parameter map. However, many smaller features, most notably bowl-shaped craters, remain warmer than their surroundings. These features mostly vanish when scattering and emission is accounted for, indicating that the elevated temperature in many bowl-shaped craters is due to topographic focusing of illumination, and does not necessarily indicate a difference in thermophysical properties. For the equatorial and mid-latitudes, our model largely removes topographic effects and the remaining spatial variations in nighttime temperature mostly indicate differences in thermophysical properties.

Figure 10 shows ΔT_{BOL} for a region at high latitudes (50°–70°N). Here, topography subtraction is less effective. Many topographic features, most notably pole-facing slopes, show up as warmer than their surroundings. This is likely due to complexities in the emission phase function that are not accounted for in our model. This can be addressed in future work when the emission phase function has been fully characterized. Additionally, our model simplifies the scattered and emitted radiation by assuming that the peak flux occurs at noon and does not account for the timing of illumination from different parts of the surrounding scene. Both effects likely cause errors at equatorial latitudes as well but are more pronounced at high latitudes where indirect illumination constitutes a larger fraction of the total illumination, and where high solar incidence angles lead to directionally anisotropic emission and scattering. However, even at high latitudes the model does partially correct for land emission and scattering when compared to the simple slope correction. Figure 10c shows less significant temperature differences due to slope than for a simple slope correction in Figure 10b.

4. Results and Discussion

4.1. Global Maps

We produce 15 maps in total, each extending to ±70° latitude and gridded at 128 ppd. These are: (a) channel 6–9 brightness temperature, bolometric temperature, and regolith temperature at midnight and slope-adjusted midnight; (b) derived RA at slope-adjusted midnight; and (c) bolometric temperature and regolith temperature
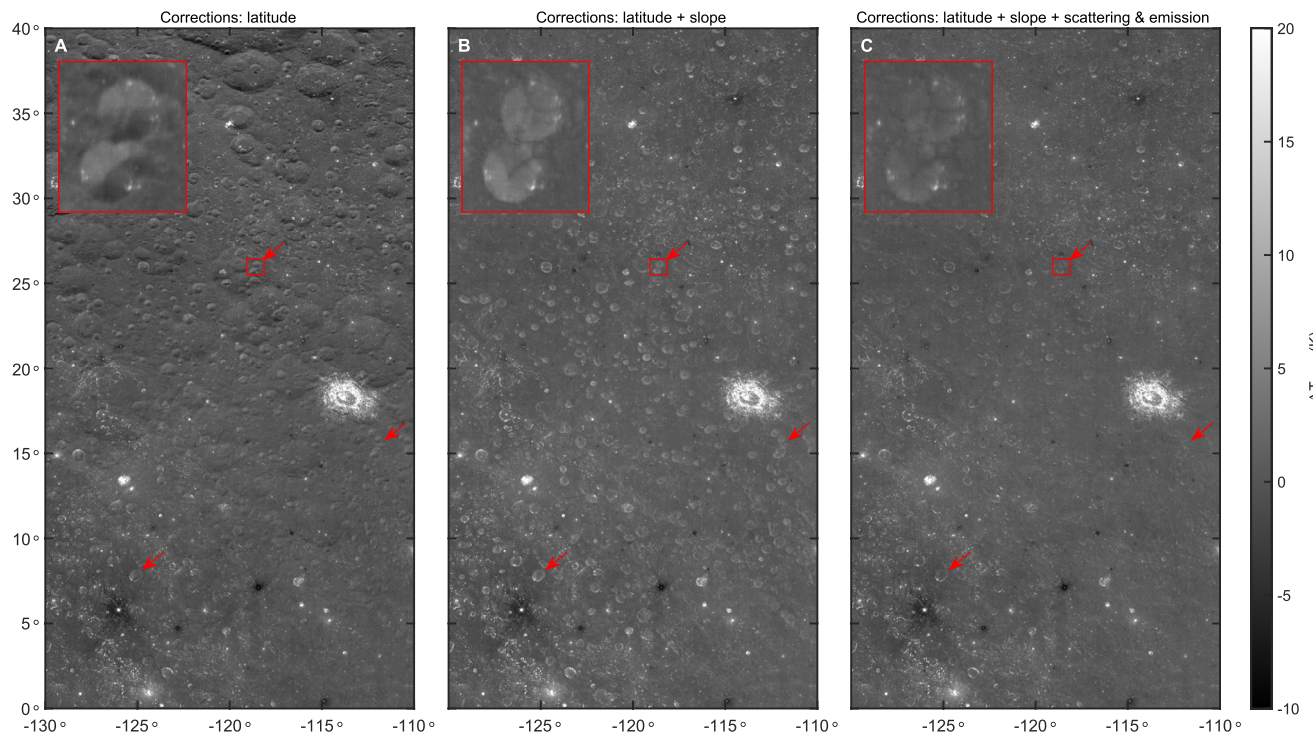
Figure 9. An example region showing midnight bolometric temperature anomaly with different levels of topographic removal: (a) correction for latitude, but no topography correction; (b) correction for latitude and slope angle, but not for scattering and emission; and (c) correction for latitude, slope angle, and scattering and emission. The red arrows show examples of bowl-shaped craters which remain warmer than their surroundings when only slope and latitude are accounted for. These features mostly vanish when scattering and emission is included. The inset figure shows a close-up of the region outlined by the red box.

anomaly at slope-adjusted midnight. Figure 11 shows examples of three of these: midnight bolometric temperature, bolometric temperature anomaly, and RA. Spatial coverage for the brightness and bolometric temperature maps is nearly complete, with only ~0.003% of spatial bins having too few observations to determine a midnight or slope-adjusted midnight temperature. Coverage is less complete for the RA, regolith temperature, and temperature anomaly maps because pole-facing slopes with effective latitudes greater than ±85° are excluded
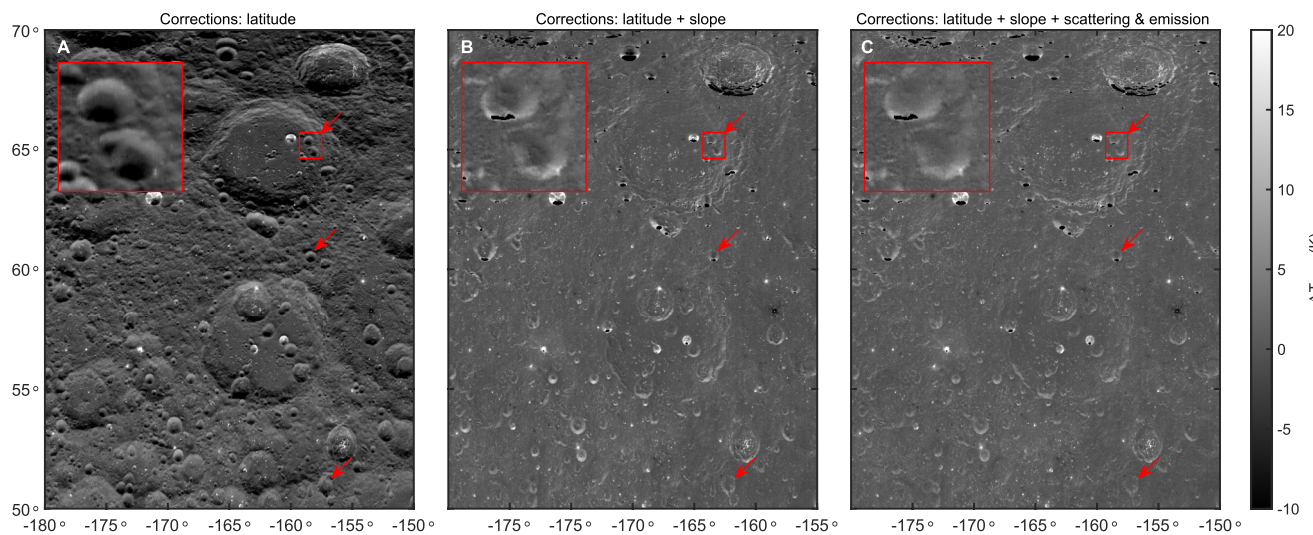

Figure 10. An example region showing midnight bolometric temperature anomaly with different levels of topographic removal. At high latitudes, topographic removal is less effective than at equatorial latitudes. The red arrows show several bowl-shaped craters which are partially but not completely removed when scattering and emission from surrounding topography is included. The inset figure shows a close-up of the region outlined by the red box.
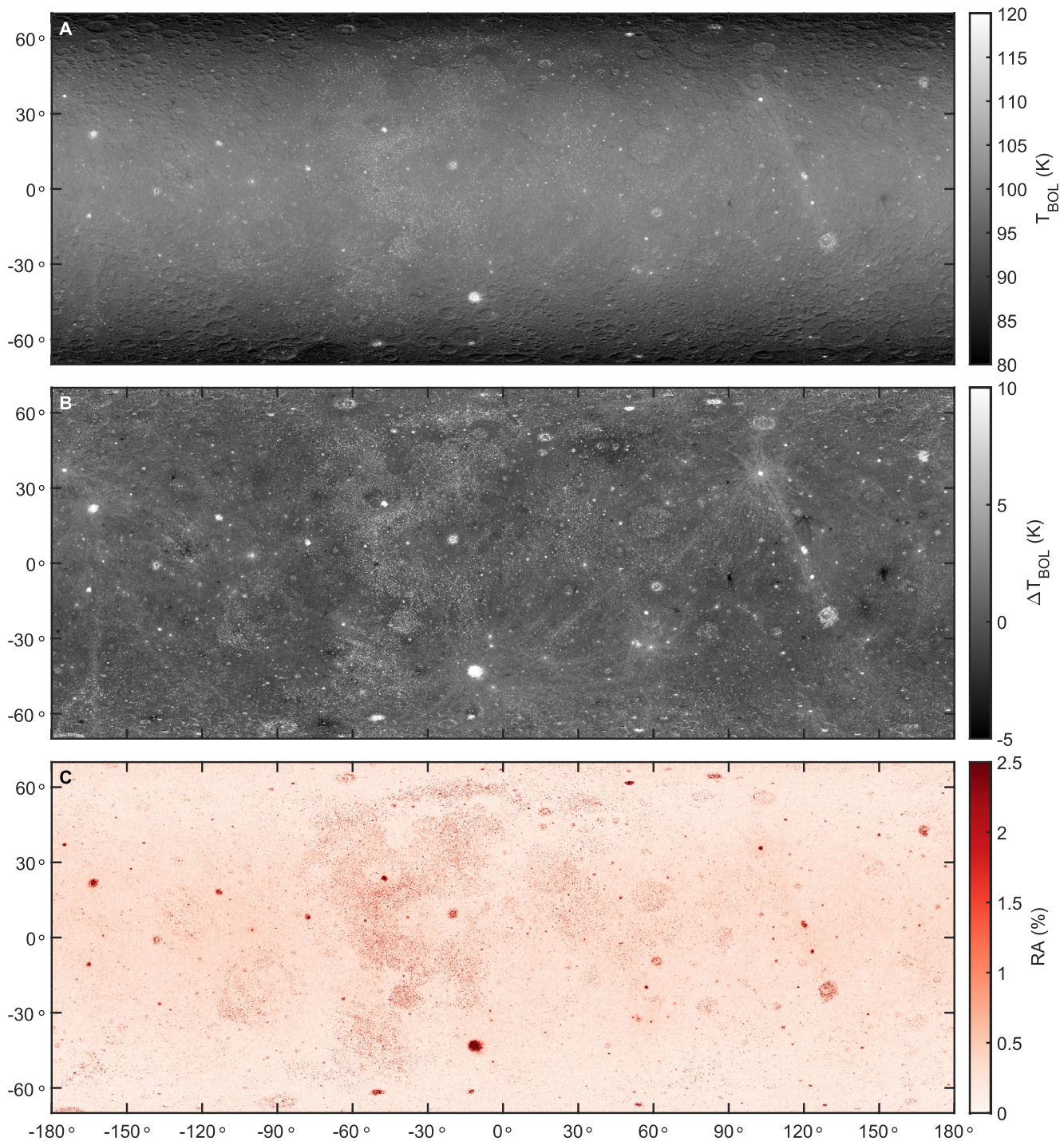
Figure 11. Global maps of (a) bolometric temperature at midnight, (b) bolometric temperature anomaly at slope-adjusted midnight, and (c) rock abundance at slope-adjusted midnight.

from the thermal modeling required to produce them. This affects ∼0.16% of spatial bins, almost all at high latitudes.

Figure 12 shows the correlation between the new RA and temperature anomaly products with their previous versions within ±50° latitude. Temperature anomaly data is constrained to flat surfaces (slope < 5°) to avoid topographic effects, which were not corrected for in the previous regolith temperature map. Rock abundance
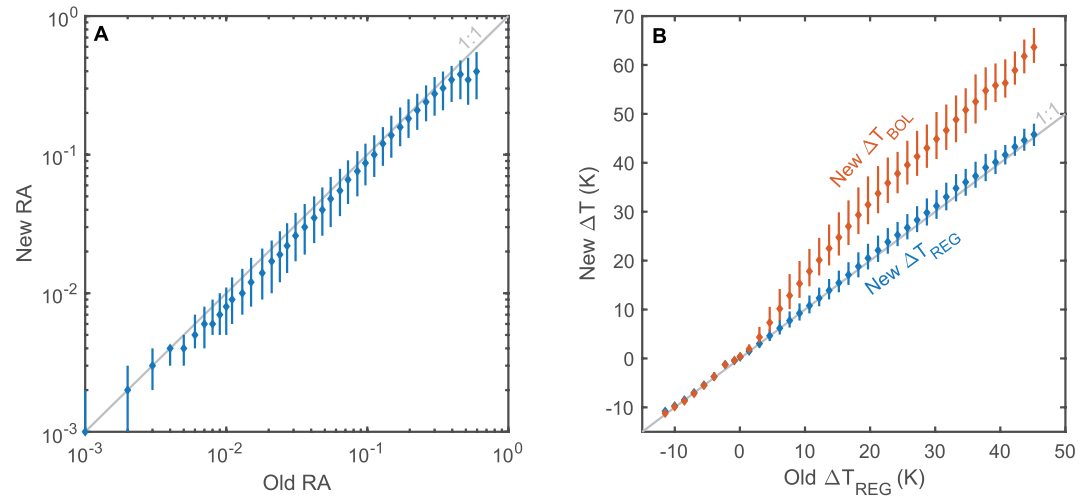
Figure 12. Cross plots comparing the new and old (a) rock abundance (RA) and (b) temperature anomaly products within ±50° latitude. Temperature anomaly data is constrained to flat surface (slope < 5°). Data points show binned medians with error bars indicating the interquartile range. The new and old RA and regolith temperatures are in very close agreement globally. Bolometric temperature is greater than regolith temperature for positive temperature anomalies.

and regolith temperature closely follow a 1:1 correlation, indicating very good agreement between the new and old data products. As expected, this demonstrates that our processing method successfully reproduces the values from the previous products. Bolometric temperature is systematically greater than regolith temperature for positive temperature anomalies. This is because warm nighttime temperatures on the Moon are typically caused by rockiness. As described in Section 2.5, the contribution of rocks is removed in the calculation of regolith temperature but included in the bolometric temperature, so regolith temperature is necessarily cooler than bolometric temperature. The difference between regolith and bolometric temperature becomes greater at higher temperatures because anomalously warm regions tend to have higher RA. Regolith and bolometric temperatures agree for negative temperature anomalies, indicating that most anomalously cold regions have generally low RA.

Lunar nighttime temperatures are sensitive to the thermophysical properties of the surface to a depth characterized by the thermal skin depth, $z_s \sim \sqrt{\kappa P / \pi}$ where κ is thermal diffusivity and P is the synodic rotational period of the Moon. This corresponds to ~4–10 cm for typical regolith and ~1 m for coherent rock. As has been noted by previous authors (Bandfield et al., 2011; Hayne et al., 2017), nighttime temperatures and derived thermophysical properties like the H-parameter on the Moon are incredibly uniform at the global scale, even across dramatically different terrain types like mare and highlands. While the mare can often be distinguished from highlands by an elevated abundance of small rocky impact craters, typical intercrater regolith in the mare and highlands have similar nighttime temperatures. This indicates that a regolith layer with a thickness at least a few times the thermal skin depth has developed across most of the Moon from billions of years of impact bombardment. The increased abundance of rocky craters in the mare is evidence that the regolith layer is thinner in the mare than in the highlands, as more frequent small impacts are able to penetrate the regolith to excavate underlying rocks (Elder et al., 2019).

4.2. Examples of Map Improvements

The primary improvements to the new Diviner maps are an increase in effective resolution due to better data georeferencing and the removal of topographic effects. These effects allow for the identification of smaller and fainter thermal features, which is best demonstrated by looking at smaller-scale example regions.

Figure 13 compares the old regolith temperature anomaly map and the new bolometric temperature anomaly map for Taurus-Littrow valley, the landing site of the Apollo 17 mission (30.77°E, 20.19°N). This example highlights that the improved georeferencing in the new maps allows smaller rocky craters to be identified than was previously possible. For example, a cluster of ~400–600 m diameter rocky craters to the south of the Apollo 17 Lunar Module (LM) appears as an unresolved region of increased nighttime temperature in the old map. In the new
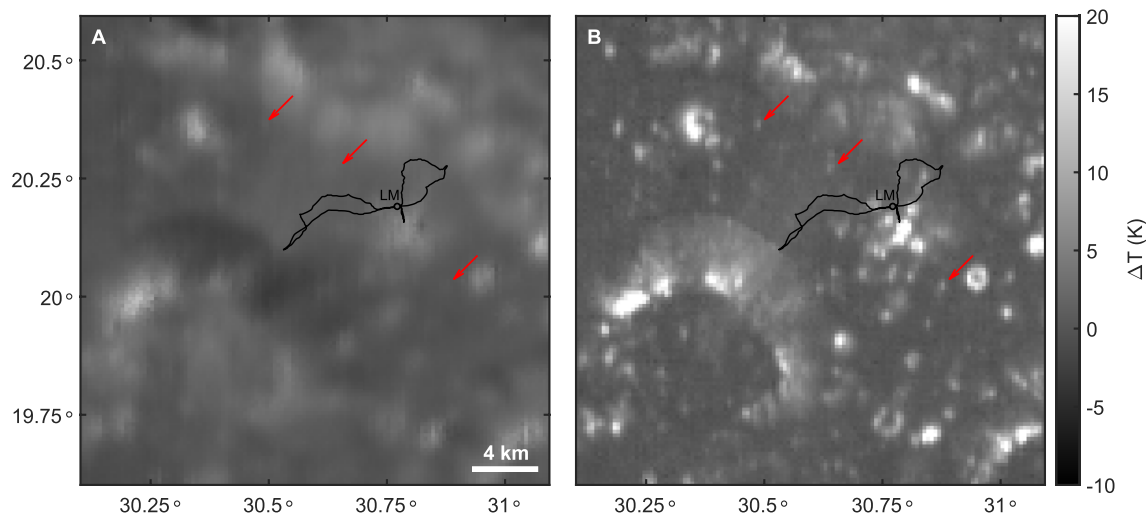
Figure 13. Comparison of (a) the previously published regolith temperature map and (b) the updated bolometric temperature anomaly map at Taurus-Littrow valley, the Apollo 17 landing site. In the previous product, a cluster of rocky craters to the south of the Apollo 17 Lunar Module appears as an unresolved region of increased nighttime temperature. In the new product, individual craters can be resolved. The red arrows show the locations of several ~200 m diameter rocky craters that do not appear in the old regolith temperature map but are identifiable in the new bolometric temperature map.

map, each crater is individually resolved, and differences in their thermophysical properties are perceptible. In addition, several smaller ~200 m diameter rocky craters throughout the region do not appear in the old map but are identifiable in the new map (indicated by the red arrows in Figure 13). One advantage of this improvement is that nighttime temperatures measured by Diviner can be better correlated with other high-resolution data sets or with surface measurements in the case of landed missions.

Large rocky impact craters are among the most prominent features in the Diviner nighttime data set. Figure 14 shows Tsiolkovskiy crater (180 km, 129.2°E, −20.4°N), which has an anomalously high RA for a crater of its age (>3.2 Ga) (Pasckert et al., 2015; Williams et al., 2013). This can be attributed to a large impact melt deposit to the southeast of the crater (Greenhagen et al., 2016). The melt deposit is more prominent and thermally distinct from the surrounding regolith in the new nighttime temperature map. This is mostly due to the improved topographic correction, as the slight increase in temperature associated with the impact melt was previously difficult to distinguish above topographic variations in temperature. The sharp, well-defined boundary between impact melt and background regolith apparent in the new maps indicates that the melt deposit is well preserved, despite its old age.

Lunar cold spots are extensive ray-like regions of reduced nighttime temperature associated with very young impact craters (Bandfield et al., 2011; Williams et al., 2018). Bandfield et al. (2014) proposed that these features can be explained by a fluffing-up of the upper centimeters of regolith out to great distances (~10–100 crater radii), resulting in a low thermal inertia layer. Figure 15 shows an example of a prominent cold spot around a ~600 m diameter crater (−131.71°E, 34.21°N). The cold spot structure has significantly more detail in the new maps, displaying a distinctive sinuous ray system. Like optical crater rays, individual cold spot rays appear to be made up of chains of smaller low thermal inertia streaks. These rays are sometimes discontinuous. For example, faint traces of a cold spot ray can be identified at distances of ~60 km or ~200 crater radii away, which was not observed in the previous map. This indicates that cold spots have a more detailed structure and extend to greater distances from their source crater than was previously known.

Figure 15 also shows a smaller cold spot around a ~150 m crater (−131.30°E, 36.38°N). The central crater and its nearby ejecta now appear as a warm feature ~1–2 pixel across. Previously this was not observed, likely due to blurring of the warm rocky crater with the surrounding cold spot.

4.3. Validating Rock Abundance With Manual Boulder Counts

A key advantage of the improvement in effective spatial resolution is that the new Diviner maps are better spatially correlated with high-resolution images. To demonstrate this, we compare the Diviner derived RA with
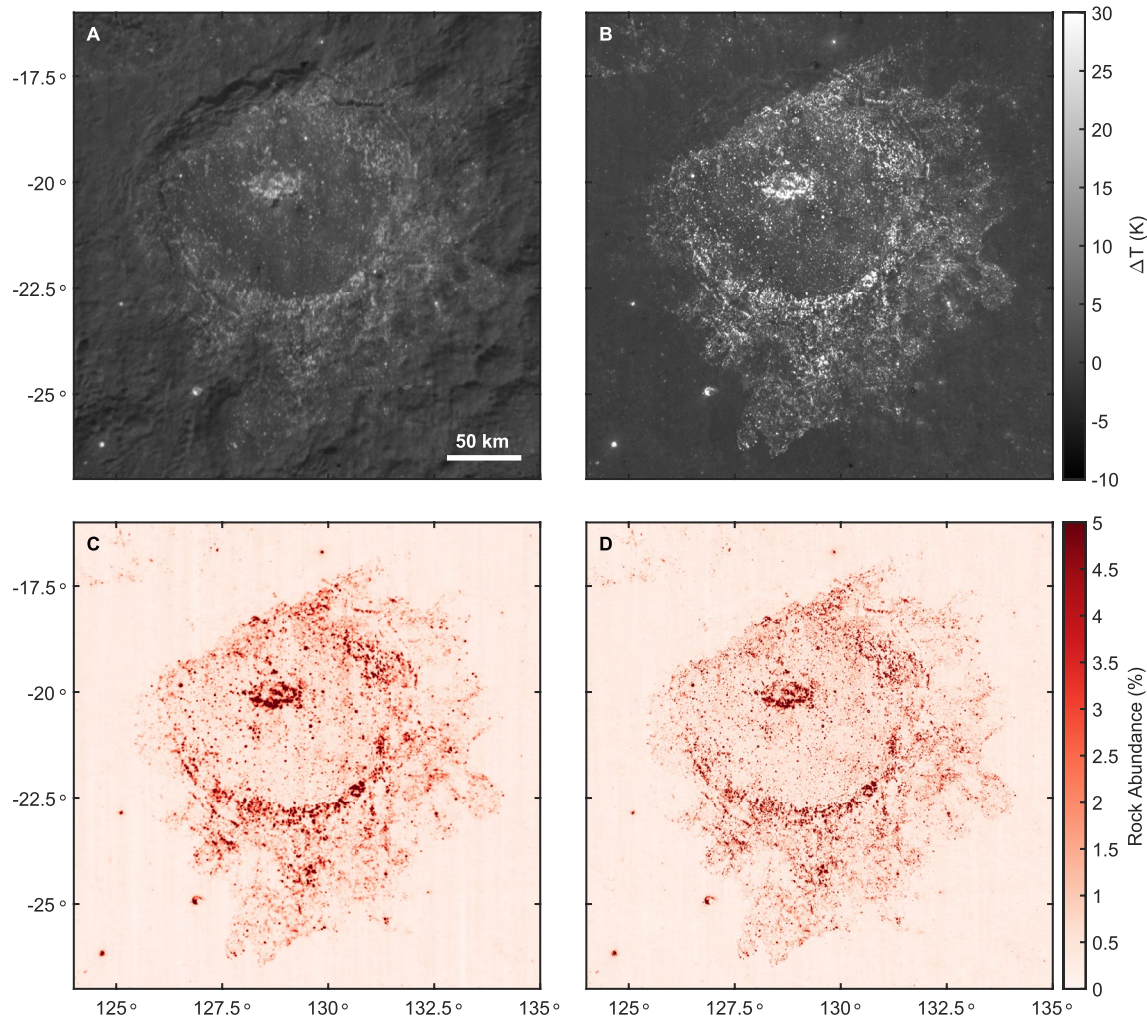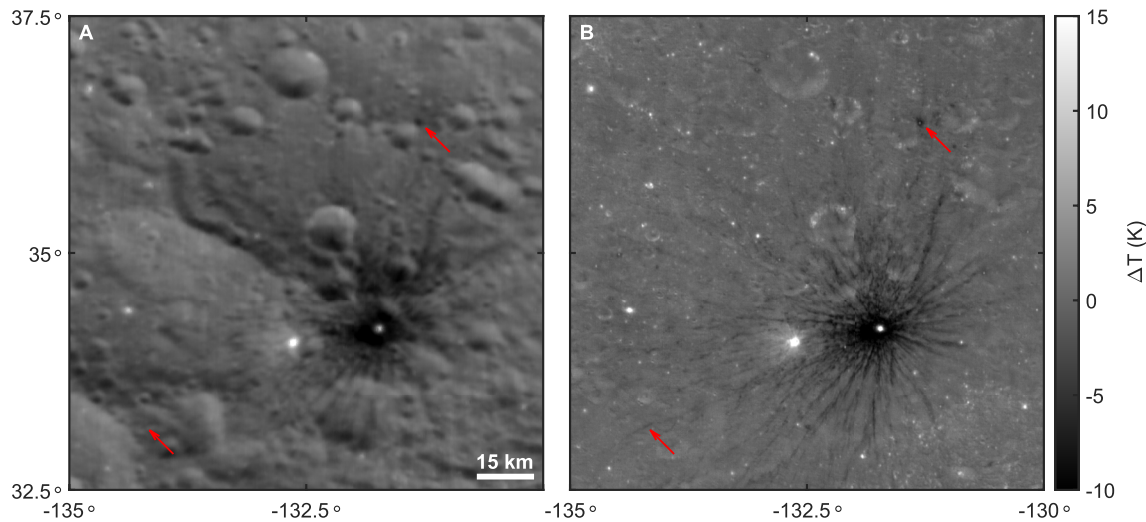
Figure 14. Comparison of the previously published (a) nighttime regolith temperature and (c) rock abundance (RA) maps with the new (b) bolometric temperature anomaly and (d) RA maps for the Tsiolkovskiy crater (129.2°E, −20.4°N). Topographic removal allows the boundary of the melt deposit to be clearly defined.

the number of boulders visible in LROC imagery for a ~4.2 by ~2.9 km region roughly centered on the Apollo 17 LM (Figure 16). This region has four craters with notable RA signatures: Camelot crater (30.731°E, 20.195°N, 625 m), Powell crater (30.763°E, 20.160°N, 412 m), Sherlock crater (30.813°E, 20.184°N, 503 m), and Steno-Apollo crater (30.794°E, 20.145°N, 520 m). Of these, Diviner measures the highest RA for Steno-Apollo crater (~0.074), an intermediate RA for Powell and Sherlock craters (~0.034), and a comparatively low RA for Camelot crater (~0.014) (Figure 16c). We manually count boulders in this region using the Apollo 17 LROC NAC Orthomosaic (Haase et al., 2019) and several additional NAC images (M113751661L, M129086118L, M129086118R, 162107606L, M165645700L, M165645700R, and M172717297R) which were selected to have resolutions of ~0.5 m/pixel and to cover a range of illumination geometries. The count region extends one 128 ppd spatial bin beyond the pictured count region. This is necessary for comparison to the RA maps because the spatial response of a Diviner spatial bin extends slightly beyond the target bin (Figure 2f). In total, we identified ~30,000 boulders in the count region.

Figure 17 shows the cumulative size-frequency distribution (SFD) of the boulder survey. We find that the boulder SFD can be described with a power-law:

$$N = C D^{-b} \tag{6}$$

where N is the cumulative number of boulders larger than diameter D, C is a coefficient describing the number of boulders of a particular size, and b is the power-law slope which controls the ratio of small boulders to large

Figure 15. Comparison of the (a) previously published nighttime regolith temperature map with the (b) new bolometric temperature anomaly map for a lunar cold spot. Topographic removal and improved sharpness allow the detailed sinuous structure of the cold spot to be visible at significantly greater distance. The left red arrow shows a faint cold spot ray streak not apparent in the previous map. The top red arrow shows a small cold spot whose ~150 m diameter central crater is apparent as warm feature ~1–2 pixels across in the new map.

boulders. For boulders larger than ~2 m in diameter, the survey SFD has a power-law slope of about −5 to −6. Figure 17 also shows the SFD of boulders located within 1.25 crater radii of the four rocky craters of interest. The boulder power-law slopes for each crater are also generally within the range of −5 to −6. Though, interestingly, the boulder SFD for Sherlock crater appears to have a shallower slope (b ~4) for boulders larger than ~3 m while maintaining a steeper slope (b ~5–6) for smaller boulders. These values generally agree with Watkins et al. (2019), who performed a survey of boulders on the ejecta blankets of several rocky craters (200–950 m) and found power-law slopes ranging from 4.4 to 6.8. For each SFD in Figure 17, the power-law behavior does not continue for boulders smaller than ~2 m. This roll-off is due to the resolution limit of NAC images, where boulders smaller than ~4 pixels across (2 m at 0.5 m/pixel) are difficult to identify. We assume that our survey is mostly complete for boulder >2 m.

Figure 16a shows the spatial density of >2 m boulders gridded at 128 ppd. There is relatively good spatial correlation between the boulder spatial density map and the Diviner RA map (Figure 16c). The spatial bins with highest boulder density, associated with Steno-Apollo crater, also have the highest Diviner RA. However, there are also some dissimilarities, mostly at the boundaries of rocky features. For example, several of the spatial bins surrounding Steno-Apollo crater have moderate RA measured by Diviner but very few counted boulders. These discrepancies likely arise because the RA of a Diviner spatial bin is also partially sensitive to boulders in neighboring spatial bins as discussed in Section 2.3. Figure 2f shows that the SRF for a spatial bin is most strongly influenced by the properties within that bin, but also includes some contribution from neighboring regions, mostly to the north and south. Therefore, the RA measured by Diviner for a particular spatial bin represents the properties of a region which is slightly larger than a single 128 ppd spatial bin. To properly compare the Diviner RA map with our manual boulder counts, we convolve the spatial density of counted boulders using the SRF for a 128 ppd spatial bin at 20°N latitude. The resulting map (Figure 16b) appears very similar to the Diviner derived RA map (Figure 16c), where spatial bins bordering rocky regions inherit some boulder density from neighboring bins.

Rock abundance represents the areal fraction of the surface covered by rocks. Therefore, we can convert boulder spatial density to a "manual RA" by summing the cross-sectional area of each rock within a spatial bin's SRF and dividing by the total area (weighted by the SRF). The blue points in Figure 18 show that there is a strong roughly linear correlation between the Diviner derived RA and the areal rock fraction of boulders >2 m in diameter. However, the coverage of >2 m boulders is systematically lower than the Diviner RA. This indicates that Diviner is sensitive to rocks smaller than 2 m, which were not reliably counted in the boulder survey because of the resolution limit of NAC images. To extend our boulder counts to smaller sizes, we extrapolate the rock counts within each spatial bin according to a power-law with a slope of −5.5, a value appropriate for the overall SFD slope in this region. We achieve the best agreement between Diviner RA and the manual RA when
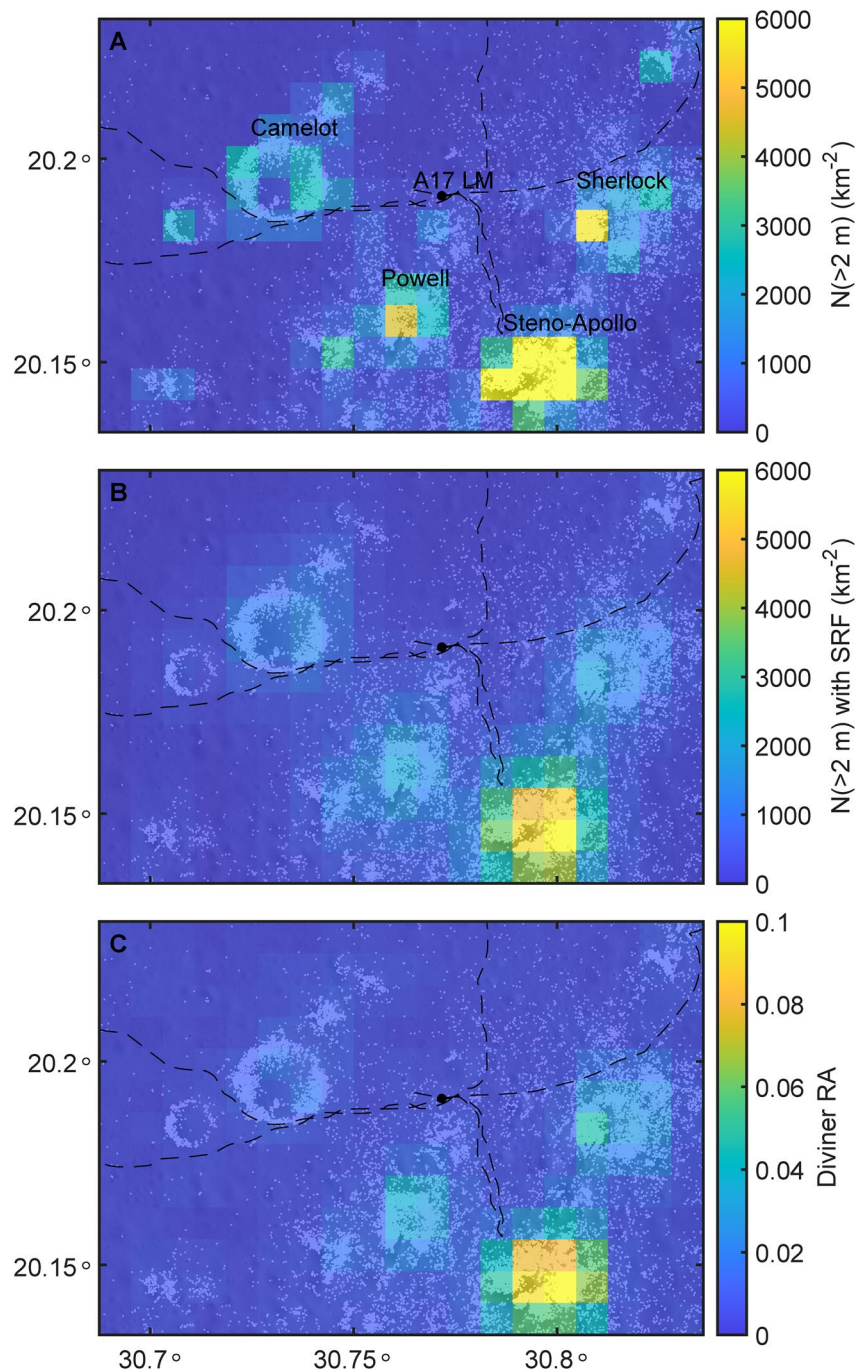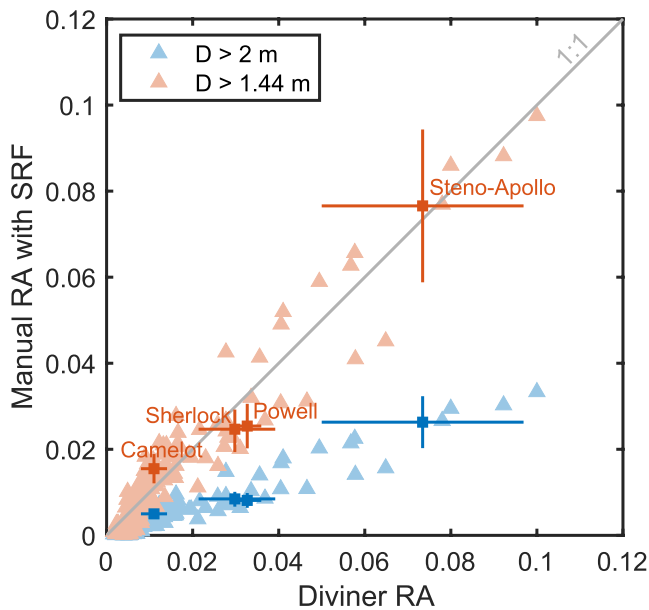
Figure 16. Comparison between manual boulder counts and Diviner rock abundance (RA) in the Apollo 17 landing site region: (a) The spatial density of counted >2 m boulders binned at 128 pixel-per-degree (ppd); (b) The spatial density of >2 m boulders accounting for the spatial response function of a 128 ppd spatial bin (Section 2.3); and (c) Diviner derived RA. The white points show boulders >1 m in diameter.

extrapolating to boulders larger than ~1.44 m in diameter (Figure 18). This value may be slightly influenced by uncertainties in boulder counting, which may affect both the number of rocks identified and the diameters assigned to each boulder. For a ±20% error in the number and diameter of counted boulders, the best fit rock size remains between ~1–2 m. This agrees with Bandfield et al. (2011), who estimated that the Diviner RA map should be sensitive to rocks sufficiently larger than the thermal skin depth for rock, which is ~1 m. Rocks
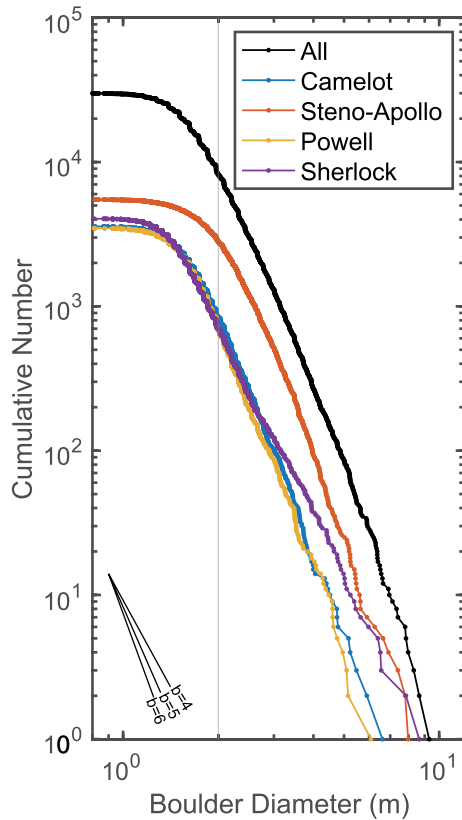
Figure 17. Cumulative size-frequency distribution (SFD) for a survey of boulders in the Apollo 17 landing site region. The colored lines show the boulder SFD within 1.25 crater radii of four rocky craters. Each SFD has a power-law slope of ~5–6.

Figure 18. Comparison between the Diviner derived rock abundance (RA) and the manual RA calculated from boulder counts, after the spatial response function is accounted for. Diviner RA best agrees with the inferred areal fraction of >~1.44 m boulders.

smaller than this experience lateral cooling from the surrounding regolith and retain less heat than larger rocks because of their lower mass, resulting in lower nighttime temperatures.

This example demonstrates that the improvements made to the georeferencing of Diviner data allow for excellent spatial correlation with high-resolution data sets, in this case LROC NAC images. The value for a particular spatial bin is influenced by the properties of a region slightly larger than that spatial bin, however this effect does not typically extend more than ~1 spatial bin away at equatorial and mid latitudes.

5. Conclusions

Using ~13 years of Diviner data, we produce updated nighttime temperature and RA maps of the Moon. In addition to greater data volume, several improvements are implemented that result in significantly sharper maps. Errors in the Diviner instrument's pointing are corrected, resulting in better georeferencing of Diviner observations. Additionally, past EFOV modeling has been optimized to improve data georeferencing without spatial interpolation. We estimate that these improvements result in an increase in the effective resolution of Diviner maps of ~3.5× longitudinally and ~1.3× latitudinally. Additionally, we develop a thermal model which accounts for topographic scattering and emission to remove the effect of topography on nighttime temperatures. Indirect illumination scattered and emitted from surrounding topography can have a significant effect on nighttime temperatures for regions which have a high percentage of land in their line of sight. By subtracting the effect of topography on nighttime temperature, we produce temperature anomaly maps that better isolate differences in thermophysical properties.

The improvement in map sharpness allows the lunar thermal environment to be studied at a finer scale than was previously possible, and topographic removal reveals faint thermal features which were previously hidden by topographic effects. We show that the elevated nighttime temperatures observed in many bowl-shaped craters can be explained by topographic scattering and emission, and does not necessarily indicate a difference in thermophysical properties. The uniformity of intercrater terrain nighttime temperatures suggests a globally ubiquitous regolith layer with a thickness that extends to at least a few diurnal skin depths regardless of surface age. We also find that the impact melt deposit around Tsiolkovskiy crater is sharper and better defined than was previously shown, in spite of its old age. Lunar cold spots have more detailed structure and extend to greater distances from their source craters than was previously known.

The improved effective resolution of Diviner maps enables better spatial correlation with other high-resolution data sets. To demonstrate this, we counted >30,000 boulders larger than ~1 m in a region near the Apollo 17 landing site using LROC imagery. Diviner derived RA strongly correlates with rock counts after accounting for the SRF of a gridded spatial bin, which can extend slightly beyond a single 128 ppd spatial bin. Diviner RA best agrees with the inferred areal coverage of rocks larger than ~1–2 m in diameter. Rocks are no longer distinguishable in Diviner RA below this threshold, thereby defining the size of a thermally distinct rock.

Data Availability Statement

The Diviner RDR data used in this study are publicly available at the Geosciences Node of the Planetary Data System (PDS) (http://pds-geosciences.wustl.edu/missions/lro/diviner.htm) (Paige et al., 2022). The 128 ppd gridded global maps generated in this study are available at the Diviner Dataverse repository at UCLA (https://doi.org/10.25346/S6/LFAVXU) (Powell, 2022). The updated maps will also be made available on the Geosciences Node of the PDS.

References

Aharonson, O., & Schorghofer, N. (2006). Subsurface ice on Mars with rough topography. *Journal of Geophysical Research*, *111*(E11), E11007. https://doi.org/10.1029/2005JE002636

Bandfield, J. L., Cahill, J. T., Carter, L. M., Neish, C. D., Patterson, G. W., Williams, J.-P., & Paige, D. A. (2017). Distal ejecta from lunar impacts: Extensive regions of rocky deposits. *Icarus*, *283*, 282–299. https://doi.org/10.1016/j.icarus.2016.05.013

Bandfield, J. L., Ghent, R. R., Vasavada, A. R., Paige, D. A., Lawrence, S. J., & Robinson, M. S. (2011). Lunar surface rock abundance and regolith fines temperatures derived from LRO Diviner Radiometer data. *Journal of Geophysical Research*, *116*(E12), E00H02. https://doi.org/10.1029/2011JE003866

Bandfield, J. L., Hayne, P. O., Williams, J.-P., Greenhagen, B. T., & Paige, D. A. (2015). Lunar surface roughness derived from LRO Diviner Radiometer observations. *Icarus*, *248*, 357–372. https://doi.org/10.1016/j.icarus.2014.11.009

Bandfield, J. L., Song, E., Hayne, P. O., Brand, B. D., Ghent, R. R., Vasavada, A. R., & Paige, D. A. (2014). Lunar cold spots: Granular flow features and extensive insulating materials surrounding young craters. *Icarus*, *231*, 221–231. https://doi.org/10.1016/j.icarus.2013.12.017

Barker, M. K., Mazarico, E., Neumann, G. A., Zuber, M. T., Haruyama, J., & Smith, D. E. (2016). A new lunar digital elevation model from the Lunar Orbiter Laser Altimeter and SELENE Terrain Camera. *Icarus*, *273*, 346–355. https://doi.org/10.1016/j.icarus.2015.07.039

Conel, J. E. (1969). Infrared emissivities of silicates: Experimental results and a cloudy atmosphere model of spectral emission from condensed particulate mediums. *Journal of Geophysical Research*, *74*(6), 1614–1634. https://doi.org/10.1029/JB074i006p01614

Elder, C. M., Douglass, B., Ghent, R., Hayne, P., Williams, J.-P., Bandfield, J., & Costello, E. (2019). The subsurface coherent rock content of the moon as revealed by cold-spot craters. *Journal of Geophysical Research: Planets*, *124*(12), 3373–3384. https://doi.org/10.1029/2019JE006128

Elder, C. M., Hayne, P. O., Piqueux, S., Bandfield, J., Williams, J.-P., Ghent, R. R., & Paige, D. A. (2016). The lunar rock size frequency distribution from diviner infrared measurements. In *Agu fall meeting abstracts* (p. P24A-04).

Foote, E. J., Paige, D. A., Shepard, M. K., Johnson, J. R., & Biggar, S. (2020). The bidirectional and directional hemispheric reflectance of Apollo 11 and 16 soils: Laboratory and Diviner measurements. *Icarus*, *336*, 113456. https://doi.org/10.1016/j.icarus.2019.113456

Greenhagen, B. T., Bandfield, J., Bowles, N. E., Hayne, P. O., Sefton-Nash, E., Warren, T., & Paige, D. A. (2017). Sideways views of the moon: Mapping directional thermal emission with diviner. In *Agu fall meeting abstracts* (p. P41D-2850).

Greenhagen, B. T., Lucey, P. G., Bandfield, J. L., Hayne, P. O., Williams, J.-P., & Paige, D. (2011). The diviner lunar radiometer compositional data products: Description and examples. In *42nd annual lunar and planetary science conference* (p. 2679).

Greenhagen, B. T., Lucey, P. G., Wyatt, M. B., Glotch, T. D., Allen, C. C., Arnold, J. A., et al. (2010). Global silicate mineralogy of the moon from the Diviner Lunar Radiometer. *Science*, *329*(5998), 1507–1509. https://doi.org/10.1126/science.1192196

Greenhagen, B. T., Neish, C. D., Williams, J.-P., Cahill, J. T., Ghent, R. R., Hayne, P. O., et al. (2016). Origin of the anomalously rocky appearance of Tsiolkovskiy crater. *Icarus*, *273*, 237–247. https://doi.org/10.1016/j.icarus.2016.02.041

Haase, I., Wählisch, M., Gläser, P., Oberst, J., & Robinson, M. S. (2019). Coordinates and maps of the Apollo 17 landing site. *Earth and Space Science*, *6*(1), 59–95. https://doi.org/10.1029/2018EA000408

Hayne, P. O., Bandfield, J. L., Siegler, M. A., Vasavada, A. R., Ghent, R. R., Williams, J.-P., et al. (2017). Global regolith thermophysical properties of the moon from the Diviner Lunar Radiometer Experiment. *Journal of Geophysical Research: Planets*, *122*(12), 2371–2400. https://doi.org/10.1002/2017JE005387

Helbig, N., Löwe, H., & Lehning, M. (2009). Radiosity approach for the shortwave surface radiation balance in complex terrain. *Journal of the Atmospheric Sciences*, *66*(9), 2900–2912. https://doi.org/10.1175/2009JAS2940.1

Horai, K.-I., & Simmons, G. (1972). Thermal property measurements on lunar material returned by Apollo 11 and 12 missions. *Progress in Astronautics and Aeronautics*, *28*, 243–267.

Horvath, T., Hayne, P. O., & Paige, D. A. (2019). Thermal environments and illumination in lunar pits and lava tubes. In *Agu fall meeting abstracts* (p. P31C-3454).

Horvath, T., Hayne, P. O., & Paige, D. A. (2022). Thermal and illumination environment of lunar pits and caves: Models and observations from the Diviner Lunar Radiometer Experiment. *Geophysical Research Letters*, *49*(14), e2022GL099710. https://doi.org/10.1029/2022GL099710

Lucey, P. G., Greenhagen, B. T., Donaldson Hanna, K., Bowles, N., Flom, A., & Paige, D. A. (2021). Christiansen feature map from the lunar reconnaissance orbiter Diviner Lunar Radiometer Experiment: Improved corrections and derived mineralogy. *Journal of Geophysical Research: Planets*, *126*(6), e2020JE006777. https://doi.org/10.1029/2020JE006777

Mazarico, E., Neumann, G. A., Barker, M. K., Goossens, S., Smith, D. E., & Zuber, M. T. (2018). Orbit determination of the lunar reconnaissance orbiter: Status after seven years. *Planetary and Space Science*, *162*, 2–19. https://doi.org/10.1016/j.pss.2017.10.004

Mazarico, E., Rowlands, D., Neumann, G., Smith, D., Torrence, M., Lemoine, F., & Zuber, M. (2012). Orbit determination of the lunar reconnaissance orbiter. *Journal of Geodesy*, *86*(3), 193–207. https://doi.org/10.1007/s00190-011-0509-4

Paige, D. A., Bachman, J. E., & Keegan, K. D. (1994). Thermal and albedo mapping of the polar regions of Mars using Viking thermal mapper observations: 1. North polar region. *Journal of Geophysical Research*, *99*(E12), 25959–25991. https://doi.org/10.1029/93JE03428

Paige, D. A., Foote, M., Greenhagen, B., Schofield, J., Calcutt, S., Vasavada, A., et al. (2010). The lunar reconnaissance orbiter Diviner Lunar Radiometer Experiment. *Space Science Reviews*, *150*(1), 125–160. https://doi.org/10.1007/s11214-009-9529-2

Paige, D. A., Siegler, M. A., Zhang, J. A., Hayne, P. O., Foote, E. J., Bennett, K. A., et al. (2010). Diviner lunar radiometer observations of cold traps in the moon's south polar region. *Science*, *330*(6003), 479–482. https://doi.org/10.1126/science.1187726

Paige, D. A., Sullivan, M. T., & Williams, J.-P. (2022). Lunar reconnaissance orbiter diviner derived data bundle 1. *NASA Planetary Data System*. https://doi.org/10.17189/WJ0S-W188

Pasckert, J. H., Hiesinger, H., & van der Bogert, C. H. (2015). Small-scale lunar farside volcanism. *Icarus*, *257*, 336–354. https://doi.org/10.1016/j.icarus.2015.04.040

Powell, T. M. (2022). Replication data for: High-resolution nighttime temperature and rock abundance mapping of the moon using the Diviner Lunar Radiometer Experiment with a model for topographic removal [Dataset]. UCLA Dataverse. https://doi.org/10.25346/S6/LFAVXU

Rosenburg, M. A., Aharonson, O., Head, J. W., Kreslavsky, M. A., Mazarico, E., Neumann, G. A., et al. (2011). Global surface slopes and roughness of the Moon from the Lunar Orbiter Laser Altimeter. *Journal of Geophysical Research*, *116*(E2), E02001. https://doi.org/10.1029/2010JE003716

Rubanenko, L., Schorghofer, N., Greenhagen, B. T., & Paige, D. A. (2020). Equilibrium temperatures and directional emissivity of sunlit airless surfaces with applications to the moon. *Journal of Geophysical Research: Planets*, *125*(6), e2020JE006377. https://doi.org/10.1029/2020JE006377

Sullivan, M. T., Paige, D. A., Arvidson, R. E., & Grayzeck, E. (2013). Lunar reconnaissance orbiter Diviner Lunar Radiometer Experiment: Reduced data record and derived products software interface specification. In *Technical report, version 1.13*. PDS Geosciences Node.

Tooley, C. R., Houghton, M. B., Saylor, R. S., Peddie, C., Everett, D. F., Baker, C. L., & Safdie, K. N. (2010). Lunar reconnaissance orbiter mission and spacecraft design. *Space Science Reviews*, *150*(1), 23–62. https://doi.org/10.1007/s11214-009-9624-4

Vasavada, A. R., Bandfield, J. L., Greenhagen, B. T., Hayne, P. O., Siegler, M. A., Williams, J.-P., & Paige, D. A. (2012). Lunar equatorial surface temperatures and regolith properties from the Diviner Lunar Radiometer Experiment. *Journal of Geophysical Research*, *117*(E12), E00H18. https://doi.org/10.1029/2011JE003987

Warren, T. J., Bowles, N. E., Donaldson Hanna, K., & Bandfield, J. L. (2019). Modeling the angular dependence of emissivity of randomly rough surfaces. *Journal of Geophysical Research: Planets*, *124*(2), 585–601. https://doi.org/10.1029/2018JE005840

Watkins, R. N., Jolliff, B. L., Mistick, K., Fogerty, C., Lawrence, S. J., Singer, K. N., & Ghent, R. R. (2019). Boulder distributions around young, small lunar impact craters and implications for regolith production rates and landing site safety. *Journal of Geophysical Research: Planets*, *124*(11), 2754–2771. https://doi.org/10.1029/2019JE005963

Williams, J.-P., Bandfield, J. L., Paige, D. A., Powell, T. M., Greenhagen, B. T., Taylor, S., et al. (2018). Lunar cold spots and crater production on the moon. *Journal of Geophysical Research: Planets*, *123*(9), 2380–2392. https://doi.org/10.1029/2018JE005652

Williams, J.-P., Greenhagen, B. T., Bennett, K. A., Paige, D. A., Kumari, N., Ahrens, C. J., et al. (2022). Temperatures of the Lacus Mortis region of the moon. *Earth and Space Science*, *9*(2). https://doi.org/10.1029/2021EA001966

Williams, J.-P., Greenhagen, B. T., Paige, D. A., Schorghofer, N., Sefton-Nash, E., Hayne, P. O., et al. (2019). Seasonal polar temperatures on the moon. *Journal of Geophysical Research: Planets*, *124*(10), 2505–2521. https://doi.org/10.1029/2019JE006028

Williams, J.-P., Paige, D. A., Greenhagen, B. T., & Sefton-Nash, E. (2017). The global surface temperatures of the moon as measured by the Diviner Lunar Radiometer Experiment. *Icarus*, *283*, 300–325. https://doi.org/10.1016/j.icarus.2016.08.012

Williams, J.-P., Petro, N. E., Greenhagen, B. T., & Neish, C. (2013). Inferred age of mare fill in Tsiolkovskiy crater: Constraints on the preservation of exterior impact melt deposits. In *44th annual lunar and planetary science conference* (p. 2756).

Williams, J.-P., Sefton-Nash, E., & Paige, D. A. (2016). The temperatures of Giordano Bruno crater observed by the Diviner Lunar Radiometer Experiment: Application of an effective field of view model for a point-based data set. *Icarus*, *273*, 205–213. https://doi.org/10.1016/j.icarus.2015.10.034

Winter, D. F., & Krupp, J. (1971). Directional characteristics of infrared emission from the moon. *The Moon*, *2*(3), 279–292. https://doi.org/10.1007/BF00561881